Plasmonics and near field optics for sensing purposes

Sara Zuccon

January 2010

Contents

List of Figures

List of Tables

List of Abbreviations and Acronyms

3-APTES   (3-Aminopropyl)-triethoxysilane

ATR   Attenuated total reflection

DMF   Dymetilformamide

FWHM   Full Width at Half Maximum

NIR   Near Infrared, wavelength: 800-2500nm

PAH   poly(allylamine hydrochloride)

PSS   poly(styrene sulfonate)

SPP   Surface Plasmon Polariton

SPR   Surface Plasmon Resonance

TIR   Total Internal Reflection

UV   Ultraviolet light, wavelength: 10-400nm

vis   visible light, wavelength: 400-780nm

Chapter 1

Introduction

We have to go back to 1902 to find the first documented observation of surface plasmons, at that time Wood illuminated a metallic diffraction grating with polychromatic light and noticed narrow dark bands in the spectrum of the diffractred light, which he referred to as anomalies[59]. As theoretical interpretation of this experimental anomalies, Fano [13] concluded that they were associated with the excitation of electromagnetic surface waves on the diffraction grating. Later in 1958 Turbadar[55] observing the reflected intensity from thin metal film on a substrate, registered a large drop in reflectivity under certain conditions, but he did not find an explanation for this fact. We have to wait 1968 when Otto demonstrated that the drop in the reflectivity in the attenuated total reflection method is due to the excitation of surface plasmons [44]. In the same year, Kretschmann and Raether reported excitation of surface plasmons in another configuration called attenuated total reflection method [32]. The pioneering work of Otto, Kretschmann and Raether established a convenient method for the excitation of surface plasmons and their investigation, and introduced surface plasmons into modern optics. In the late 1970s, surface plasmons were first employed for the characterization of thin films [46] and the study of processes at metal boundaries [20].

For their peculiar characteristics surface plasmons are widely used for the de-

sign of optical sensors. An optical sensor is a device which, by optical means, converts a quantity being measured to another quantity (output) which is in general encoded into one of the characteristics of a light wave. In surface plasmon based sensors, the plasmon is excited at the interface between a metal film and a dielectric medium (superstrate), changes in the refractive index and thickness of the latter modify the resonance condition of the plasmon. This technique is indeed usually used to measure film parameters. In particular a change in the refractive index of the superstrate produces a change in the propagation constant of the surface plasmon. This change alters the coupling condition between a light wave and the surface plasmon, which can be detected as a change in one of the characteristic of the reflected light wave [27]. Based on the light wave characteristic to be sensed, sensors are classified as SPR sensors with angular, wavelength, intensity, phase or polarization modulation.

The theoretical basis of surface plasmon excitation will be described in the first paragraphs of the present thesis. Now an overview of the just mentioned different kind of SPR sensors is presented. In SPR sensors with angular modulation[37] a monochromatic light wave excites a surface plasmon. The strength of coupling between the incident wave and the surface plasmon is observed at multiple angles of incidence of the light wave. The reflected intensity is meaured and usually the angle of incidence yielding the strongest coupling, which means a drop in reflectivity, is recorded and used as sensor output. In SPR sensors with wavelength modulation[62] a surface plasmon is excited by a collimated light beam containing multiple wavelengths. The angle at which the light wave is incident onto the metal film is kept constant. The wavelength showing the strongest coupling to surface plasmon (reflectivity minimum) is measured and used as sensor output. In SPR sensors with intensity modulation[43], the sensor output is the intensity (proportional to reflectivity), it measures the strength of the coupling for a fixed wavelength

at a single angle of incidence. In SPR sensors with phase modulation[5] the shift in phase of the light wave interacting with the SP is measured at a single angle of incidence and wavelength of the light wave and used as a sensor output. In SPR with polarization modulation[33], changes in the polarization of the light wave interacting with a surface plasmon are measured.

As it has already been demonstrated Surface Plasmon Resonance sensors are highly sensitive to small changes in the refractive index with resolution up to 10^{-5} RUI (refractive index unit)[28, 1, 58]. Despite this high sensitivity there has been still little work in gas and chemical detection. Hence particular attention has been paid to the development of a suitable sensing layer over the metal film. Different approaches can be found in literature, for example Maciak [35] proposed the use of WO3 thin films as active layers for NH3 vapor detection. Other approaches include organic material [14], polymeric films [52], composites[16] or hybrid organic and inorganic[51, 36]. On the track of the works of Manera[36] and Rella[51] we have tested the capabilities of TiO2 for sensing purposes. The TiO2 layer has been deposited by the sol-gel technique, which provides an high porosity of the film. We then performed measurements of surface plasmon resonance. The high porosity of the films increases the interaction surface between the gas and the sensing medium, hence it improves the sensitivity. The sensitivity of these type of films has been tested on different kinds of organic vapors (methanol, ethanol and isopropanol)[63].

A similar experimental configuration has been exploited in a context different from plasmonics. At the Max Plank Institute for Polymer Research a study on the behavior of the local field at the interface between two dielectrics has been carried out. Local field effects are in general calculated assuming a "dipole-like" model of the matter, in such description a molecule is considered as a dipole and the interaction with the local field is hence treated as an interaction dipole-electric field [31]. Previous studies [48, 47]have been

carried out on the fluorescence at dielectric interfaces, in order to evaluate the reliability of such description. The interface between two lossless dielectric is of particular importance because dielectrics introduce no additional energy sinks. In proximity of a metal interface part of the energy is dissipated in the metal. The presented technique uses a property of total internal reflection called evanescent wave. A beam of light is passed through a dielectric prism in such a way that it reflects once off the internal surface. This reflection in TIR conditions forms an evanescent wave which extends some hundreds nanometers away from the surface (dependent on the wavelength of the incoming light). This evanescent field is expected to interact with the sample on the outer side of the prism face. Two ways are proposed to detect this small absorption, in both cases a beam chopper and a lock-in amplifier are used, this combination improves the signal-to noise ratio in an optical measurement. The first approach is based on a fast modulating angle technique [18, 3, 7, 17, 25, 26, 45], the second is based on the so called "mirage effect" and it's resembling some already experimented techniques of thermal lensing [2, 10] or photothermal deflection spectroscopy (PDS)[61, 60, 53, 49, 42, 41, 34, 19, 11]. PDS measures the change in refractive index due to heating of a medium by absorption of light.

Chapter 2

Theory Surface Plasmon Resonance

2.1 Surface plasmons

Surface Plasmon Resonance (SPR) originates from the more general field of plasmonics. The latter is concerned with conduction electrons at metal surfaces and their interaction with electromagnetic radiation. The quantization of the collective oscillations of electrons in the conductive band of a metal originates the plasmon. Three different kinds of plasmon are possible: volume plasmons, surface plasmon polaritons and localized surface plasmons. Volume plasmons are the excitation of the conduction electron sea that occurs in bulk metals, surface plasmon polariton (SPP) originates when a surface plasmon couples with a photon and localized surface plasmons are the excitations (non-propagating) of conduction electrons in metallic nanostructures coupled to the electromagnetic field. The focus herein will be placed on surface plasmon resonance (SPR), this physical process can occur when plane-polarized light hits a metal film under total internal reflection conditions. The process has been known for a long time and exploited for sensing

purposes. In figure 2.1 an instantaneous picture of collective electron oscilla-
tions (plasmons) propagating along the metal surface, with an electric field
in the dielectric material and electrical charges moving in the plasma at the
metal surface. The minus (−) signs represent areas where there is a large
density of electrons, and the plus (+) signs represent areas where there is a
lower density of electrons. The electric field in the dielectric decays exponen-
tially with distance from the surface.
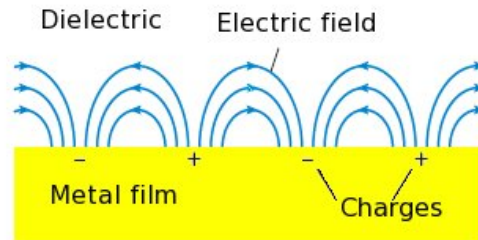
Figure 2.1: Schematic representation of an electron density wave propagating
along a metal/dielectric interface. The charge density oscillations and associated
electromagnetic fields are called surface plasmon-polariton waves

At an interface between two transparent media of different refractive in-
dex (glass and water), light coming from the side of higher refractive index
is partly reflected and partly refracted. Above a certain critical angle of inci-
dence, no light is refracted across the interface, and total internal reflection
is observed. While incident light is totally reflected the electromagnetic field
penetrates a short (tens of nanometers) distance into a medium of a lower
refractive index creating an exponentially decaying evanescent wave. If the
interface between the media is coated with a thin layer of metal (gold), and
light is monochromatic and p-polarized, the intensity of the reflected light is
reduced at a specific incident angle producing a sharp drop in the reflected

intensity (called surface plasmon resonance) due to the resonance energy transfer between evanescent wave and surface plasmons. The resonance conditions are influenced by changes in the optical properties of the system, leading to a measurable response to monitor processes near the interface.

2.2 Electromagnetic theory of surface plasmons

A possible approach to study physical properties of metals is to consider free electrons in the metal as an high density liquid, neglecting, in first approximation, the lattice. In the present section firstly the theoretical background of electromagnetic waves and their interaction with metallic surface is presented[4].

In general, the dielectric constants of both adjacent media can be complex:
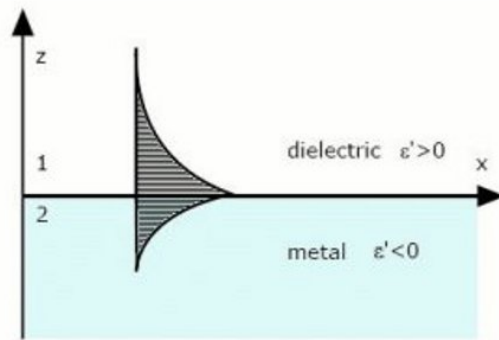
Figure 2.2: Schematic representation of a surface plasmon at the interface between metal and dielectric. Note that the dielectric constants of the two media have to be of opposite sign in order to allow for plasmon excitation.

$$\widetilde{\varepsilon}_1 = \varepsilon_1' + i\varepsilon_1''; \tag{2.1}$$

$$\widetilde{\varepsilon}_2 = \varepsilon_2' + i\varepsilon_2''; \tag{2.2}$$

Assuming the magnetic permeability equal to 1, the dielectric constant ε and the complex refractive index $(n + \imath k)$ of the materials result to be linked by the following relations.

$$
\begin{aligned}
(n + \imath k)^2 &= \varepsilon' + \imath\varepsilon''; \\
\varepsilon' &= n^2 - k^2; \\
\varepsilon'' &= 2nk;
\end{aligned}
\tag{2.3}
$$

where n is the refractive index of the material, k the absorption coefficient which describes the damping of the propagating electromagnetic wave. The two representations are equivalent.

We have to solve Maxwell equations in order to get knowledge of the electromagnetic field behavior in both media.

$$
\left.
\begin{aligned}
\overrightarrow{E}_1(\overrightarrow{r}, t) &= \overrightarrow{E}_1 \cdot exp\left(\imath\left(\widetilde{k}_{x1}x + \widetilde{k}_{z1}z\right)\right) \\
\overrightarrow{H}_1(\overrightarrow{r}, t) &= \overrightarrow{H}_1 \cdot exp\left(\imath\left(\widetilde{k}_{x1}x + \widetilde{k}_{z1}z\right)\right)
\end{aligned}
\right\} \quad for \ z > 0;
\tag{2.4}
$$

$$
\left.
\begin{aligned}
\overrightarrow{E}_2(\overrightarrow{r}, t) &= \overrightarrow{E}_2 \cdot exp\left(\imath\left(\widetilde{k}_{x2}x + \widetilde{k}_{z2}z\right)\right) \\
\overrightarrow{H}_1(\overrightarrow{r}, t) &= \overrightarrow{H}_1 \cdot exp\left(\imath\left(\widetilde{k}_{x2}x + \widetilde{k}_{z2}z\right)\right)
\end{aligned}
\right\} \quad for \ z < 0;
\tag{2.5}
$$

here $\widetilde{k}_{x1}, \widetilde{k}_{x2}, \widetilde{k}_{z1}, \widetilde{k}_{z2}$ are the wave vectors for media 1 and 2 in the x and z directions respectively.

The problem is symmetric in the y direction, so the electromagnetic fields can be separated into transverse magnetic (TM, p-polarization) modes with $\overrightarrow{H} = (0, H_y, 0)$ and transverse electric (TE, s- polarization) modes with $\overrightarrow{E} = (0, E_y, 0)$. All other solutions are superpositions of these two cases.

The electric field in s-polarization has no component perpendicularly to the interface, so it can't excite any surface polariton. The excitation of surface

polaritons is only possible in p-polarization. The continuity of the tangential components of the electric field, E, and magnetic field, H, has to be imposed as boundary condition:

$$E_{x1} = E_{x2},$$
$$H_{y1} = H_{y2} \qquad (2.6)$$

Substituting (2.4) and (2.5) into the above relations, it follows $k_x = k_{x1} = k_{x2}$. Through the Maxwell's equations one gets:

$$\widetilde{k}_{z1}H_{y1} - \frac{\omega}{c}\widetilde{\varepsilon}_1 E_{x1} = 0,$$
$$\widetilde{k}_{z2}H_{y2} - \frac{\omega}{c}\widetilde{\varepsilon}_2 E_{x2} = 0. \qquad (2.7)$$

The boundary conditions in (2.6) lead the only non trivial solution

$$\frac{\widetilde{k}_{z1}}{\widetilde{k}_{z2}} = -\frac{\widetilde{\varepsilon}_1}{\widetilde{\varepsilon}_2} \qquad (2.8)$$

Such an electromagnetic wave can exist only at he interface between two media with dielectric constants of opposite sign (see figure 2.2). It means that plasmons can be excited at the interface between metal layers (negative ε') and dielectrics.

The dispersion relation of surface plasmons can be derived from the previous presented equations:

$$\widetilde{k}_x = k'_x + \imath k''_x = \frac{\omega}{c_0}\sqrt{\frac{\widetilde{\varepsilon}_1\widetilde{\varepsilon}_2}{\widetilde{\varepsilon}_1 + \widetilde{\varepsilon}_2}}. \qquad (2.9)$$

The amplitude of the electric field decays exponentially into both media in the z-direction as well as in the propagation direction. The propagation length can be calculated by

$$L_x = \frac{1}{2k''_x} \qquad (2.10)$$

In applications in surface plasmon microscopy, this parameter influences the lateral resolution; L_x limits the dimensions of the smallest structures that can be detected by this method. For example for an interface between gold ($\widetilde{\varepsilon}_2 = -12 + \imath 1.1$)and air ($\widetilde{\varepsilon}_1 = 1$), and a laser wavelength of $\lambda = 632.8\ nm$, the propagation length results $L_x = 11.5\ \mu m$.

2.3   Surface plasmons excitation

Surface plasmons can be exited by electrons, but excitation through light is more easily experimentally realized. The first condition to be fulfilled is that the light has to be p-polarized. Anyway surface plasmons excitation needs particular methods for coupling with light radiation, since for the same energy, plasmons have greater wave vector respect to the light. This means that the surface plasmon dispersion curve, $\omega(k)$, lies at the right side of the light dispersion curve 2.3, as also can be seen from the following relation:

$$\frac{\omega}{c}\sqrt{\widetilde{\varepsilon}} < \frac{\omega}{c_0}\sqrt{\frac{\widetilde{\varepsilon}_1\widetilde{\varepsilon}_2}{\widetilde{\varepsilon}_1+\widetilde{\varepsilon}_2}}$$
$$\Downarrow \tag{2.11}$$
$$k_{ph} < k_{sp}$$

k_{ph} represent the wave vector of the phonon, while k_{sp} refers to the plasmon.

Since the dispersion curves do not intersect it is not possible to match the wave vector of the surface plasmons to the wave vector of incident electromagnetic radiation (light, for our purposes) in air. (This is why these surface plasmons are called non radiative, they cannot propagate into empty space.) But if, for a given frequency ω, the magnitude of the wave vector k of the light incident on the metal-air boundary can be increased, the dispersion
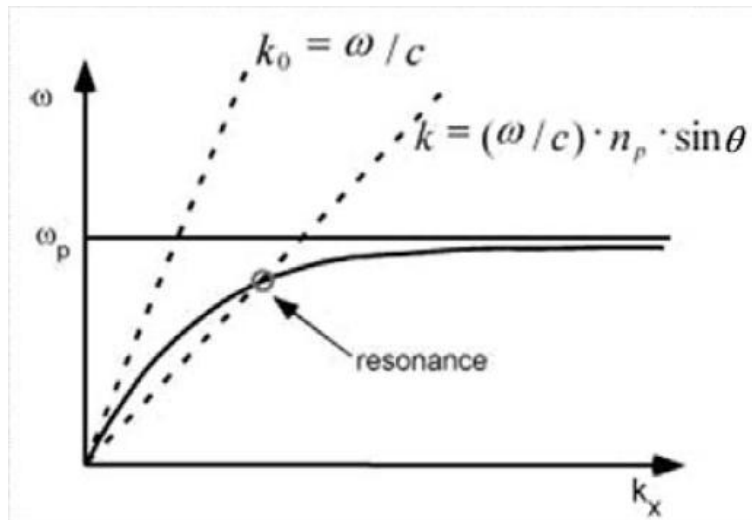
Figure 2.3: Dispersion curves for surface plasmons, air ($k_0 = \omega/c$) and glass ($k_0 = (\omega/c)n_p sin\theta$). Note that the curves do not intersect for air and plasmons, indicating that plasmons cannot be excited from light propagating from air to the metal surface.

curves will intersect.

Physically this can be accomplished by passing the incident light through a medium such as glass, on which a metal film is deposited. The glass has the effect of multiplying the wave vector by n_p, the index of refraction of glass (the index p stands for prism, as will be understood later); see figure 2.3. Then, the thin metal film of proper thickness allows some of the incident light to be transmitted through to the metal-air boundary, where the surface plasmons are excited.

The wave vector could be increased also by other techniques, for example through grating coupling. In the rest of this paragraph the most common configurations are presented.
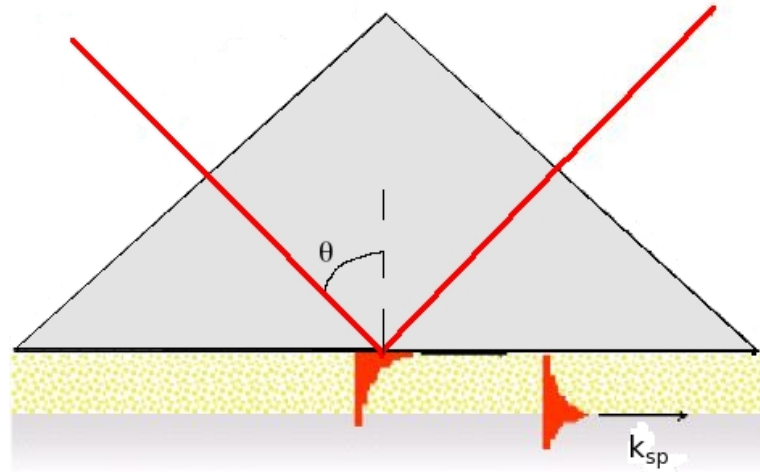
Figure 2.4: Schematic layout of the Kretschmann configuration for ATR method. The thin metal film (thickness 50 nm) is evaporated onto the base of a glass prism and acts as a resonator driven by the photon field

2.3.1 Prism coupling

The most common approach for exciting surface plasmons is the attenuated total reflection method (ATR) by means of a prism coupler. ATR uses the evanescent wave concept of total internal reflection (TIR) to measure the variations that occur when a total internally reflected light beam interacts with a sample. There are two possible exploitation of ATR: the Kretschmann and the Otto configuration respectively. In the Kretschmann geometry a high refractive index prism with refractive index n_p is directly in contact with a thin metal film with permittivity ε_m and thickness q; the metal film faces a semi-infinite dielectric medium, whose refractive index is n_d ($n_d < n_p$), see figure 2.4.

When a light wave propagating in the prism impinges onto the metal film, a part of the light is reflected back into the prism and part of it propagates in the metal as an electromagnetic wave [4]. This electromagnetic wave decays

exponentially in the direction perpendicular to the prism-metal interface, this is called evanescent wave. If the metal layer is thin enough (i.e. $q < 100\ nm$ for the visible and near infrared region of the spectrum), the evanescent wave propagates through the metal film and couples with a surface plasmon at the outer boundary of the metal film. The propagation constant of a surface plasmon propagating along a thin metal film is influenced by the presence of the dielectric on the opposite side of the metal film and can be expressed as

$$\beta^{sp} = \beta_0^{sp} + \Delta\beta = \frac{\omega}{c}\sqrt{\frac{\varepsilon_d\varepsilon_m}{\varepsilon_d + \varepsilon_m}} + \Delta\beta, \tag{2.12}$$

where β_0^{sp} represent the propagation constant of the surface plasmon propagating along the metal-dielectric interface (waveguide) in the absence of the prism. The term $\Delta\beta$ accounts for the finite thickness of the metal film and the presence of the prism. In order for coupling to happen it is necessary that the propagation constant of the evanescent wave equals the one of the surface plasmon, it means

$$\begin{gathered} \beta^{EW} = Re\{\beta^{SP}\} \\ \Downarrow \\ \frac{2\pi}{\lambda}n_p sin\theta = Re\left\{\frac{\omega}{c}\sqrt{\frac{\varepsilon_d\varepsilon_m}{\varepsilon_d+\varepsilon_m}} + \Delta\beta\right\} \end{gathered}. \tag{2.13}$$

In terms of effective index the condition is

$$\begin{gathered} n_{ef}^{EW} = Re\{n_{ef}^{SP}\} \\ \Downarrow \\ n_p sin\theta = Re\left\{\frac{\omega}{c}\sqrt{\frac{\varepsilon_d\varepsilon_m}{\varepsilon_d+\varepsilon_m}}\right\} + \Delta n_{ef}^{SP} \end{gathered}, \tag{2.14}$$

In the previous equation n_{ef}^{EW} is effective index of the evanescent wave, n_{ef}^{SP} the effective index of the surface plasmon andΔn_{ef}^{SP} takes into account
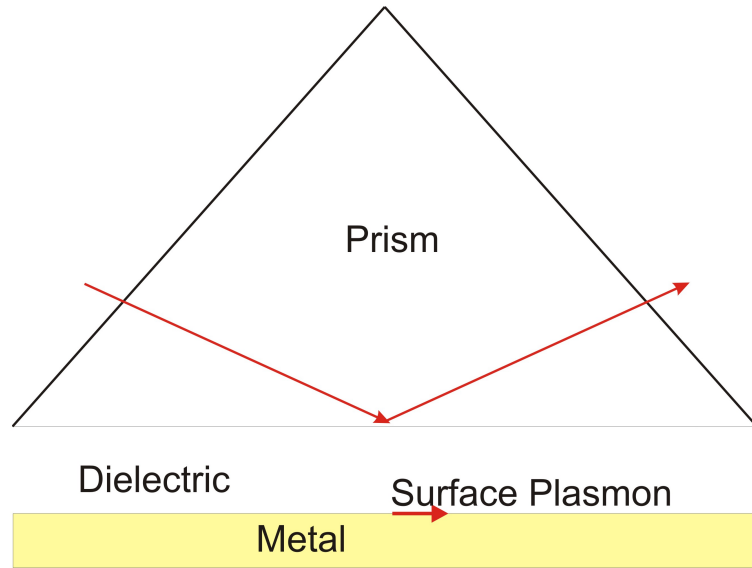
Figure 2.5: Schematic layout of the Otto geometry for coupling surface plasmons. Also in this case the surface plasmon propagates along the metal/dielectric interface

the perturbative term: $\Delta n_{ef}^{SP} = Re\left\{\lambda\Delta\beta/2\pi\right\}$.

In the Otto geometry [44] (see figure 2.5) the high refractive index prism (n_p) is interfaced with a metal-dielectric waveguide consisting of a thin dielectric film (refractive index $n_d < n_p$, thickness q) and a semi-infinite metal (ε_m).

In this configuration a light wave incident on the prism-dielectric interface with an angle greater than the critical angle for this two media produces an evanescent wave which propagates along the interface between the prism and the dielectric film. If the thickness is chosen appropriately (few microns), the evanescent wave can couple to a surface plasmon at the dielectric metal interface. The coupling condition is that the propagation constants of the evanescent wave and of the surface plasmon are equal.
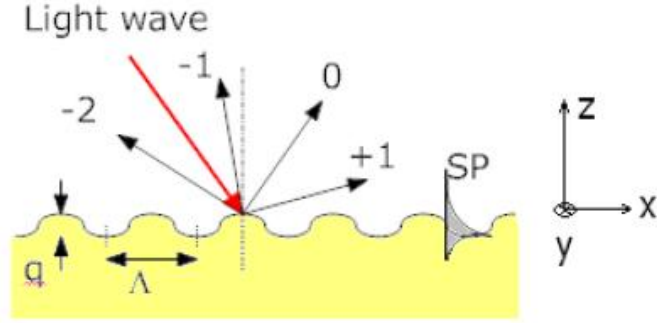
Figure 2.6: Schematic layout of grating coupling for surface plasmon excitation. The wave vector is increased by the spatial frequency.

2.3.2 Grating coupling

Another traditional approach to optical excitation of surface plasmons is based on the diffraction of light on a diffraction metal grating. In this method, a light wave is incident from a dielectric medium with refractive index n_d on a metal grating with dielectric constant ε_m, the grating period Λ and a grating depth q, see figure 2.6

When a light wave with the wave vector k is made incident on the surface of the grating, diffraction gives rise to a series of diffracted waves. The wave vector of the diffracted light k_m is [30]:

$$k_m = k + mG, \qquad (2.15)$$

Where m is the diffraction order, an integer, and G is the grating vector. G lies in the plane of the grating and is perpendicular to the grooves of the grating:

$$G = \frac{2\pi}{\lambda} x_0. \qquad (2.16)$$

The component of the wave vector of the diffracted light perpendicular to the grating plane k_{zm} is equal to the one of the incident wave, while the

component parallel to that plane is subject to diffraction k_{xm}:

$$k_{xm} = k_x + m\frac{2\pi}{\lambda} \tag{2.17}$$

The diffracted waves can couple [50] with a surface plasmon when the propagation constant of the diffracted wave propagating along the grating surface k_{xm} and that of the surface plasmon β_{SP} are equal:

$$\frac{2\pi}{\lambda}n_d sin\theta + m\frac{2\pi}{\lambda} = k_{zm} = \pm Re\left\{\beta^{sp}\right\}, \tag{2.18}$$

where

$$\beta^{sp} = \beta^{sp0} + \Delta\beta = \frac{\omega}{c}\sqrt{\frac{\varepsilon_d\varepsilon_m}{\varepsilon_d + \varepsilon_m}} + \Delta\beta \tag{2.19}$$

where β^{sp0} represent the propagation constant of the surface plasmon along a smooth interface, $\Delta\beta$ accounts for the presence of the grating. The same expression can be written in terms of effective index as previously done for prism coupling. The theoretical investigation of the interaction of the light wave with the metal grating need Maxwell's equations to be solved.

2.3.3   Waveguide coupling

Surface plasmons can be also excited by modes of a dielectric waveguide. In the figure 2.7 an example of dielectric waveguide integrating a metal-dielectric waveguide is represented. The principle of operation could be summarize in this way: when a mode propagating along the waveguide enters the region in contact with a thin metal film, it penetrates through the metal film and couples with a surface Plasmon at the outer boundary of the metal.

The coupling between the waveguide mode and a surface Plasmon can occur when the propagation constant of the mode β_M matches the real part of the propagation constant of the surface plasmon β_{SP}:

$$\beta_M = Re\left\{\beta_{sp}\right\}. \tag{2.20}$$
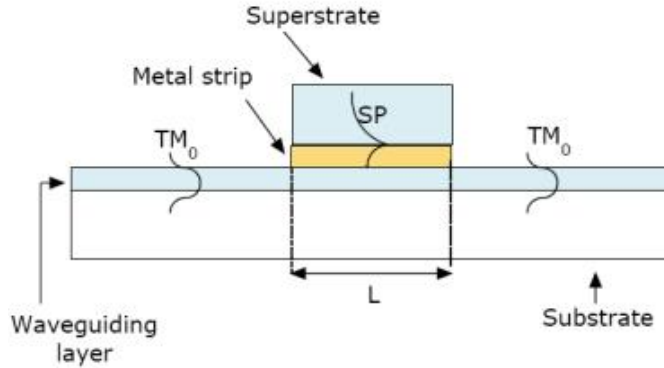
Figure 2.7: Schematic layout of the system for coupling of surface plasmon (SP) with waveguide modes (TM)

Surface plasmons are in general much more dispersive than modes of common dielectric wave guides, it follows that the resonance condition, eq. (2.20) is fulfilled only for a narrow range of wavelengths. Therefore the excitation of a surface plasmon can be observed as a narrow dip in the spectrum of transmitted light as a function of wavelength.

2.3.4 Theoretical calculation of the SPR response for prism coupling

Theory The interaction between a light wave and a surface plasmon in the ATR method can be investigated using the Fresnel multilayer reflection theory [9, 8]. In the present paragraph the analysis of the reflectivity for the Kretschmann configuration of the ATR method is presented, so to understand the model with which the MATLAB routine to calculate the SPR response has been developed. Consider a N-layer model as the one shown in figure 2.8 z_i represent the boundaries.

The tangential fields at the first boundary $z = z_1 = 0$ are related to those
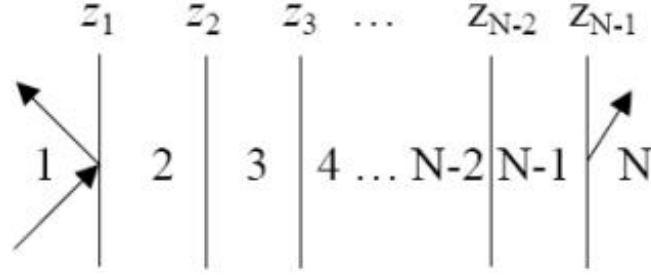
Figure 2.8: N-layer system model. Each layer is characterized by a thickness and a refractive index

at the final boundary $z = z_{N-1}$ by

$$\begin{bmatrix} U_1 \\ V_1 \end{bmatrix} = M_2 M_3 ... M_{N-1} \begin{bmatrix} U_{N-1} \\ V_{N-1} \end{bmatrix} = M \begin{bmatrix} U_{N-1} \\ V_{N-1} \end{bmatrix} \tag{2.21}$$

For p-wave at boundary k,

$$\begin{aligned} U_k &= H_y^T + H_y^R \\ V_k &= E_x^T + E_x^R \end{aligned} \tag{2.22}$$

and

$$M_k = \begin{bmatrix} \cos\beta_k & -\imath\sin\beta_k / q_k \\ -\imath q_k \sin\beta_k & \cos\beta_k \end{bmatrix} \tag{2.23}$$

where $\mu_k \simeq 1$

$q_k = (\mu_k / \tilde{\varepsilon}_k)^{1/2} \cos\theta_k \simeq \dfrac{\left(\tilde{\varepsilon}_k - n_1^2 \sin^2\theta_1\right)^{1/2}}{\tilde{\varepsilon}_k}$

$\beta_k = \frac{2\sqrt{pi}}{\lambda_0} \tilde{n}_k \cos\theta_k (z_k - z_{k-1}) = \frac{2\sqrt{pi}}{\lambda_0} (z_k - z_{k-1}) \left(\tilde{\varepsilon}_k - n_1^2 \sin^2\theta_1\right)^{1/2}$

The reflection and transmission coefficients for p-wave (TM) are respectively r_p and t_p. They can be related to the reflectivity, R_p, and transmissivity T_p by means of an opportune phase factor, respectively ϕ_p^r and ϕ_p^t. The relations between these quantities are expressed in the following formulas:

$$r_p = \frac{(M_{11}M_{12}q_N)q_1 - (M_{21}M_{22}q_N)}{(M_{11}M_{12}q_N)q_1 + (M_{21}M_{22}q_N)}$$

$$M_{ij} = \left(\prod_{k=2}^{(N-1)} M_k \right)_{ij}$$

$$R_p = |r_p|^2$$

$$r_p = R_p^{1/2} e^{\iota \phi_p^r}$$

$$\phi_p^r = \arg(r_p) \qquad (2.24)$$

$$t_H^p = \frac{2q_1}{(M_{11}M_{12}q_N)q_1 + (M_{21}M_{22}q_N)}$$

$$t_E^p = \frac{\mu_N n_1}{\mu_1 \tilde{n_N}}$$

$$T_p = \frac{\mu_N Re\left(\tilde{n_N} \cos\theta_N / \tilde{n_N}^2 \right)}{\mu_1 n_1 \cos\theta_1 / n_1^2} |t_{pH}|^2$$

$$\phi_p^t = \arg(t_{pE})$$

For s-wave (TE) the above equations hold except that the wave vector is

$$q_k = (\tilde{\varepsilon} / \mu_k)^{1/2} \cos\theta_k \qquad (2.25)$$

Implementing these equations for example in a Matlab routine it is possible to calculate the multilayer optical problem. This is what I've done. In the following paragraph some more details about the simulation model adopted are explained.

Notes on the simulation model adopted   Particular attention in the code development had to be paid for angle transformation and attenuation of the beam, due to partial reflection of the beam at the air-prism interface (surface A in figure 2.9). From now on the index of refraction of the air is idicated as n_{air}, n_p will be the one of the prism and ϕ_i and ϕ_t will be respectiveli the angle of incidence and transmission at the first prism interface . In figure 2.9 the situation is outlined.

The Snell law state that:

$$n_{air} \sin\phi_i = n_p \sin\phi_t \qquad (2.26)$$
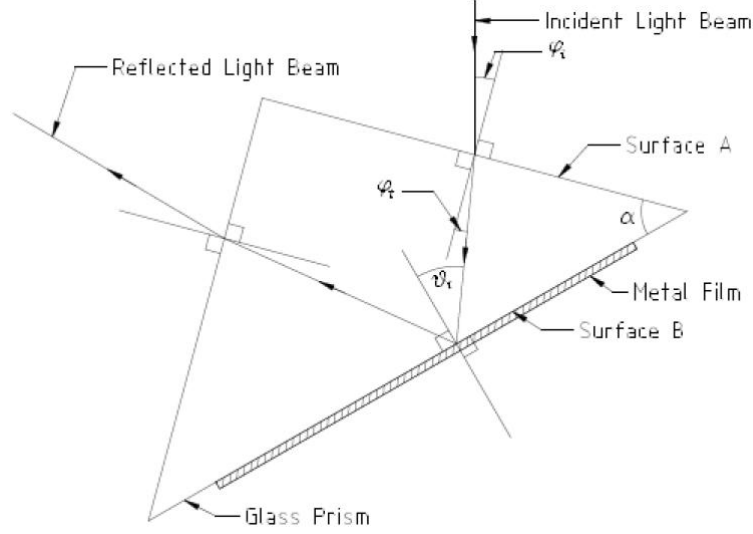
Figure 2.9: Geometry of SPR prism. Light beam entering at surface A at angle ϕ_i is refracted so that it hits the sensing layer at surface B at angle θ_i.

$$\theta_i = \alpha - \phi_t \qquad (2.27)$$

Usually a rectangular prism is employed, so that $\alpha = \pi/4$. In order to investigate the influence of the different parameters on the SPR response, some simulations are presented in the following graphs. In the figure 2.10 the reflectivity as function of wavelength and incidence angle is reported. The structure considered in this simulation is a BK7 prism, a gold film (thickness 52nm) and air on the outer side.

The angular reflectivity spectra exhibit distinct dips that are associated with the transfer of energy from the incident light wave into a surface plasmon and its subsequent dissipation in the metal film. The angle at which this dips are evident is called resonance angle.

In figure 2.12 we have fixed the wavelength at $\lambda = 635\ nm$ and varied systematically the thickness of the metal film (Au) in the range $d = 35 \div 65\ nm$. We can notice that around $d = 50\ nm$ there is the deepest minimum. This thickness is usually chosen when working at this wavelength.
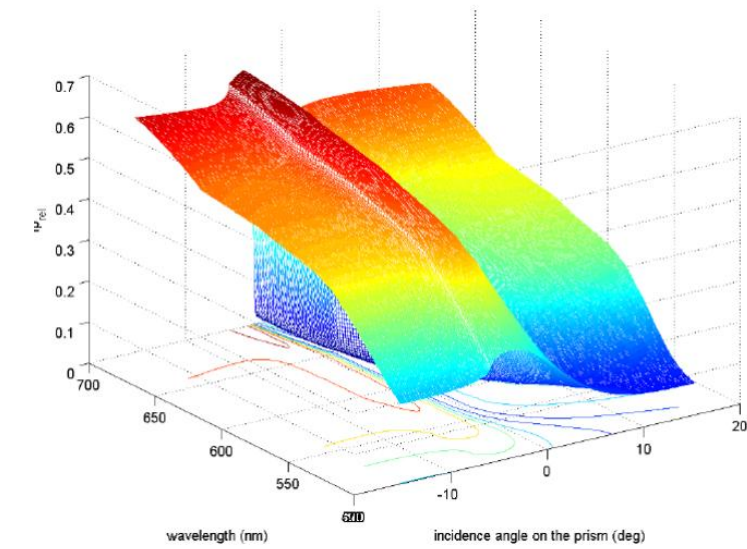
a.
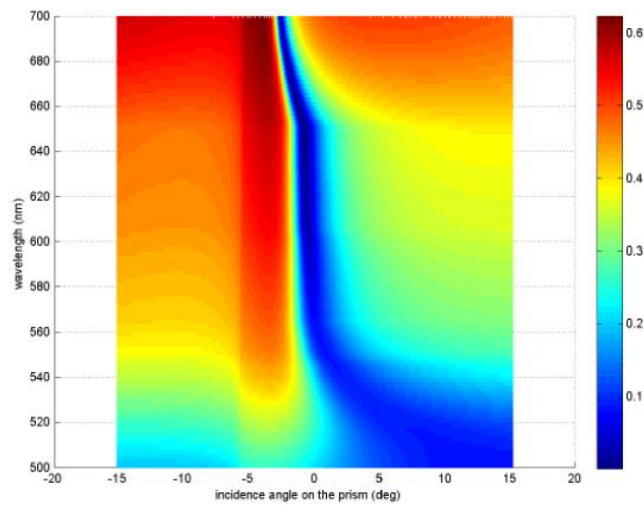
b.

Figure 2.10: Simulation reflectivity versus wavelength and angle of incidence. In a. a 3d graph is presented, while in b. the reflectivity value is displayed through colors.
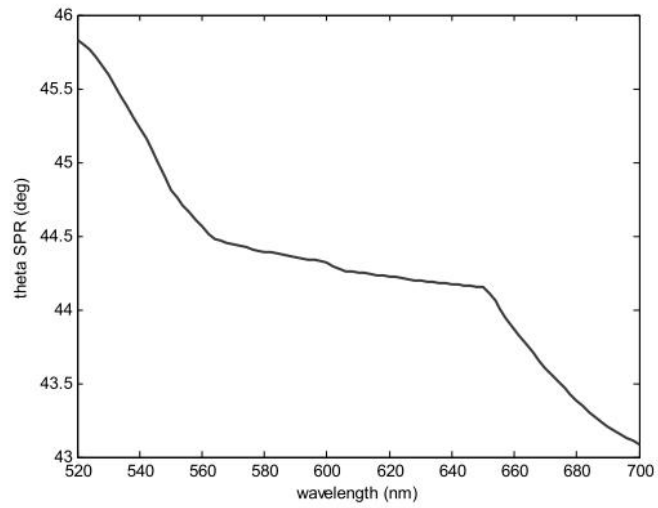
Figure 2.11: Resonance angle as a function of wavelength for the same structure as above.
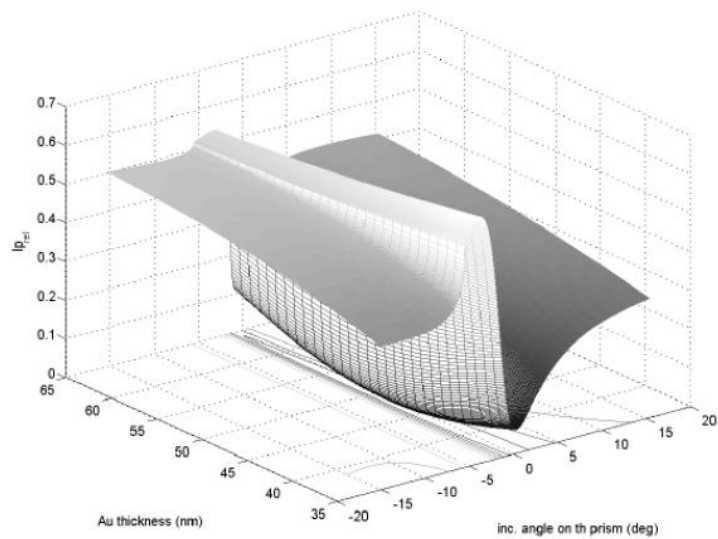
a.
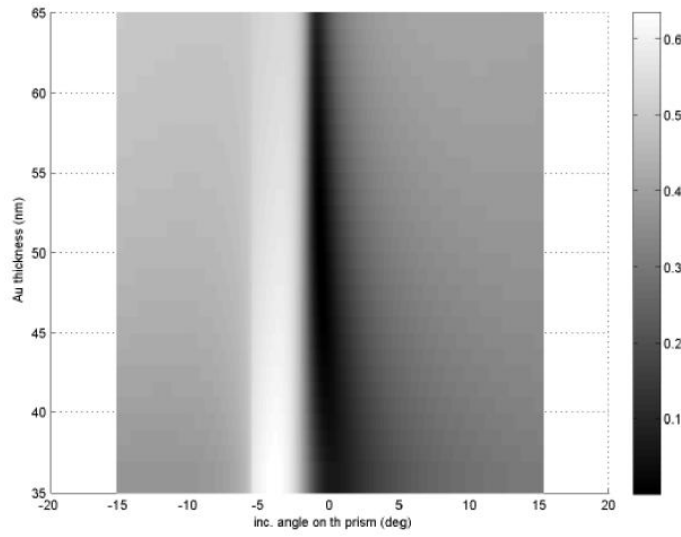
b.

Figure 2.12: Simulation reflectivity versus metal thickness and angle of incidence. In a. a 3d graph is presented, while in b. the reflectivity value is displayed through colors.

Other calculations are aimed to verify the performance of a bimetallic structure composed by a silver core and a gold superstrate. They are usually used in research and commercial applications because of their sensitivity and stability, respectively. In figure 2.13 the calculation for the reflectivity as a function of wavelength are reported for different ratios of thicknesses of the two metal layers $d(Ag)/d(Au)$.

From the calculations it is evident that the resonance deep is narrower than in the previous case. The ideal case, in terms os resolution, would be to have a pure silver film. The drawback is the instability in air of this metal. Moreover gold is more sensitive to variations in the refractive index.

a.

b.

Figure 2.13: Simulation reflectivity versus ratio Ag/Au thickness and angle of incidence. In a. a 3d graph is presented, while in b. the reflectivity value is displayed through different grey graduation.

2.3.5 Sensitivity

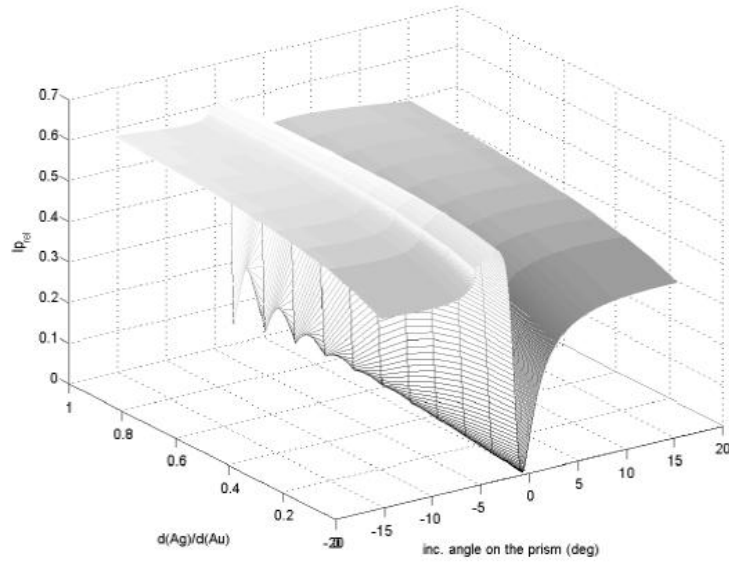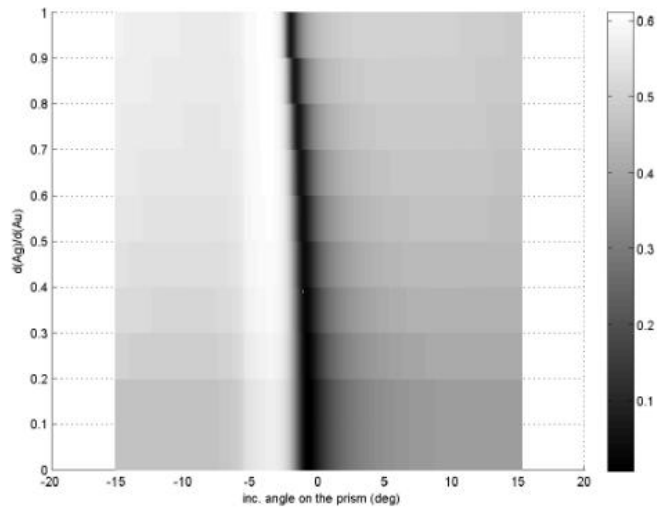The shape of the resonance curve (intensity reflected as function of the incidence angle or light wavelength) depends on the dielectric constants of material composing the prism and the sensing layer (Ag, Au, TiO_2), and on the refraction index of the substance on the free face of the metal. In the following analysis we consider the case in which the reflected intensity is recorded as a function of the incidence angle on the prism surface. It follows that once the structure has been defined, the SPR curve can be characterized by principally three parameters: minimum position, minimum height and FWHM. Once defined the structure the position is more sensitive to the real part of the refraction index of the adjacent medium, therefore this is the quantity it is commonly used in this kind of sensors. The absorption of the medium instead influences the minimum height.

Experimentally in scanning angle spectroscopy, there are two ways to monitor reaction at interfaces: dynamical response of the system, where one fixes the angle at the point of maximum slope and monitor the change in reflectivity as the reaction at the interface takes place; the other way is to compare the SPR curves in different situations, for example before and after a certain reaction. Usually these prrocedures are used in combination.

In the first situation for example one firstly measure the SPR response with air, then finds the point of maximum slope, sets the angle at this point and afterwards monitors the reflected intensity as a function of time. A change in sensed medium refractive index causes a change in reflected intensity.

Instead in the second case one is not interested in dynamical response, SPR curves are measured in both conditions. This is our case. In this case it is instead necessary to consider errors that could be introduced by mechanical movements and that can effect the repeatability of the measurement. Anyway since we have the entire curve, we have more constraints on each detected point, in this way it is possible to reduce uncertainty on the mea-

surement. In the present analysis this procedure is considered.

System efficiency as a sensor is mainly determined by three quantities: sensitivity, resolution and dynamical range. The sensitivity of a SPR transducer can be defined as the minimum change in the ambient refractive index which can be detected. It means that for the same refractive index change, a system where the minimum shift is higher has a grater sensitivity. Resolution is defined the minimum difference of the sensed parameter which can be discerned through the experimental assembly. This parameter is mainly influenced by the FWHM (full width at half maximum) of the minimum. Sensor resolution depends also from the accuracy with which SPR parameter can be monitored and so it is limited by system noise. Dynamical range is the range of sensed parameter values which can be measured from the experimental setup.

In SPR sensors with angular modulation, in order to get a theoretical estimate of the system sensitivity, we have to minimize the resonance condition respect to the scanning angle. For the simpler system prism (n_p), metal layer (ε_{mr}) and analyzed medium (n_a), it results:

$$S_{p\theta} = \frac{d\theta}{dn_a} = \frac{\varepsilon_{mr}\sqrt{-\varepsilon_{mr}}}{(\varepsilon_{mr} + n_a^2)\sqrt{\varepsilon_{mr}(n_a^2 - n_p^2) - n_a^2 n_p^2}} \qquad (2.28)$$

Applying the above relation on the considered systems, we can obtained a theoretical estimate of the system sensitivity as a function of the sensed substance refractive index or the light wavelength, as it is shown in the following graphs.

From the presented graphs it is evident that at an enough large wavelength, the sensitivity, S, becomes stable. Under these conditions one could demonstrate that the sensitivity principally depends on the contrast between the refractive index of the prism and the one of the sensed medium, i. e. it increases as the contrast diminishes. This is the reason why SPR is more sensitive when monitoring liquids (see $n_{H2O} = 1.33$) respect to gas-sensing (see
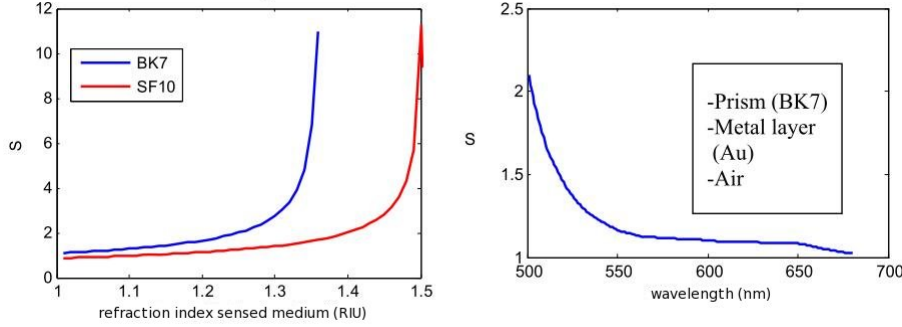
Figure 2.14: Sensitivity (rad/RIU) as a function of refractive index and sensed medium and as a function of light wavelength.

$n_{air} = 1$), since the prism material usually has a refractive index of around 1.4, 1.5. Sensitivity is also dependent on the metal used. For example gold (Au) is more sensitive of silver (Ag), as will be seen later on.

2.3.6 SPR for the characterization of thin layers adsorbed on the metal film

The evanescent field decays exponentially into the dielectric medium, so chances in the optical properties of the adjacent dielectric alter the excitation conditions for plasmons. Therefore, processes near the metal surface like the adsorption of additional dielectric layers can be sensed by the plasmon field and monitored via the resulting changes in the resonance angle of the system. Suppose to add an additional dielectric layer onto the gold. Its dielectric constant is assumed to be higher than that of the surrounding medium. Then the effective refractive index of the region sensed by the evanescent plasmon field is increased. It follows that the dispersion relation is shifted at higher values:

$$k_{p2} = k_{p1} + \Delta k \tag{2.29}$$

k_{p2}, k_{p1} represent respectively the wave vector before and after the adsorp-

tion of the added layer respectively; Δk stands for wave vector increment, it depends on both the refractive index and thickness of the additional dielectric layer.

At a given frequency ω_L of the incoming light, the intersection of dispersion relations is shifted to higher values. Consequently the resonance angle has changed. This minimum resonance shift is of fundamental importance for experimental application in methods like surface Plasmon spectroscopy or microscopy. In non adsorbing layers ($\varepsilon'' \approx 0$) the measured shift $\Delta\theta$ is proportional to the change in the optical layer thickness Δd and its contrast with the environment, i.e., the difference Δn between the film refractive index and that of the surrounding dielectric medium. For infinitesimal Δn and Δd one can write:

$$\Delta\theta \propto \Delta n \cdot \Delta d \qquad (2.30)$$

There are an infinite number of combinations of refractive index and thickness changes that lead to the same resonance shift, therefore one of the parameters has to be known (assumed or determined through other methods) in order to estimate the other.

Chapter 3

Theory Chromophores

3.1 Fluorescence

The electronic states of most organic molecules can be divided into singlet states and triplet states. In a singlet state all electrons in the molecule are spin-paired, while in a triplet state one set of electron spins is unpaired. When a molecule absorb a photon an electron from a vibrational level in the ground state is promoted to an unoccupied vibrational level in the electronic excited state. The molecule is then said to be in an excited state. This excited state is usually the first excited singlet state. A molecule in a high vibrational level of the excited state will quickly fall to the lowest vibrational level of this state by losing energy to other molecules through collision. The molecule will also partition the excess energy to other possible modes of vibration and rotation. Fluorescence occurs when the molecule returns to the electronic ground state, from the excited singlet state, by emission of a photon. If a molecule which absorbs UV radiation does not fluoresce it means that it must have lost its energy some other way. These processes are called raditionless transfer of energy. These transitions are depicted in the diagram in figure 3.1.
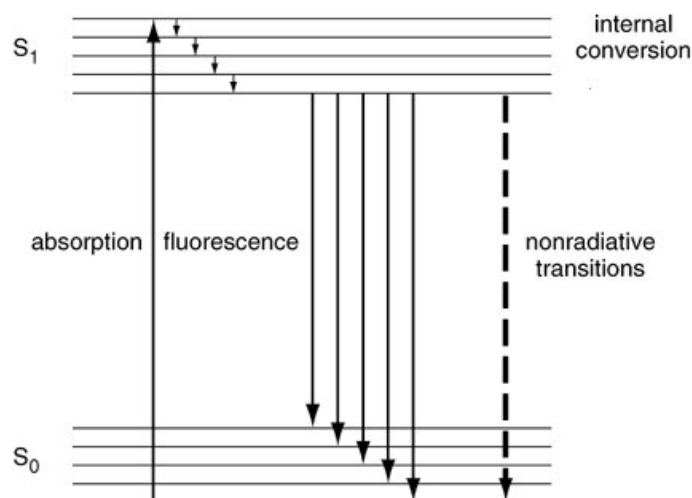
Figure 3.1: Schematic representation of the possible physical processes following absorption of a photon by a molecule

Radiative and non-radiative transitions   The excitation process can be translated in the following relation $S_0 + h\nu_{ex} \rightarrow S_1$. The fluorescent emission can be instead seen as $S_1 \rightarrow S_0 + h\nu_{em} + heat$, here $h\nu$ is a generic term for photon energy with h the Planck's constant and ν the frequency of light. S_0 represent the ground state of the fluorescent molecule and S_1 is its first excited state. A molecule in its excited state, S_1, can relax by various competing pathways. It can undergo 'non-radiative relaxation' in which the excitation energy is dissipated as heat (vibrations) to the solvent. Excited organic molecules can also relax via conversion to a triplet state which may subsequently relax via phosphorescence or by a secondary non-radiative relaxation step. Relaxation of an S1 state can also occur through interaction with a second molecule through fluorescence quenching. There are different possible mechanisms of de-excitation, some of them don't cause the emission of photons. In the internal conversion mechanism the excess energy is converted to vibrational energy, and so the molecule is placed in an extremely high vibrational level of the electronic ground state. This excess vibrational

energy is lost by collision with other molecules (vibrational relaxation). The conversion of electronic energy to vibrational energy is helped if the molecule is not tight and relaxed, because it can reorient itself in ways which aid the internal transfer of energy. A combination of intra- and inter-molecular energy redistribution is also possible. This is called intersystem crossing. In this case the spin of an excited electron can be reversed, leaving the molecule in an excited triplet state. The triplet state is of a lower electronic energy than the excited singlet state. The probability of this happening is increased if the vibrational levels of these two states overlap. For example, the lowest singlet vibrational level can overlap one of the higher vibrational levels of the triplet state. A molecule in a high vibrational level of the excited triplet state can lose energy in collision with solvent molecules, leaving it at the lowest vibrational level of the triplet state. It can then undergo a second intersystem crossing to a high vibrational level of the electronic ground state. Finally, the molecule returns to the lowest vibrational level of the electronic ground state by vibrational relaxation. this is also a non radiative decay channel which can lead to the production of heat.

Quantum yield   The fluorescence quantum yield (ϕ_F) is the ratio of photons absorbed to photons emitted through fluorescence. In other words the quantum yield gives the probability of the excited state being deactivated by fluorescence rather than by another, non-radiative mechanism. Quantum yield can be defined by equation

$$\phi_F = \frac{photons\ emitted}{photons\ absorbed} \tag{3.1}$$

Dipole model   In order to describe the excitation and relaxation processes a classical physics equivalent can be used; it consist in a parallelism between the molecule behavior and the electric dipole moment. In this picture the molecule is modeled as a couple of oscillating point-like electric dipoles. Each

one of these dipoles is associated to a specific physical process, in fact one is defined as excitation dipole moment and the second as emission dipole moment. The two dipoles may coincide if the excitation and emission processes occur from the same energy levels, while they are in general different when different levels are involved. Within this model when the dipole is irradiated by light, it starts to oscillate transferring part of this energy to the emission dipole moment. The latter, analogous to an optical antenna, will lose its energy coming back to rest by damped harmonic oscillations and emitting electromagnetic radiation in space, i.e. fluorescence radiation. in the present work we will not deal with fluorescent light, so we're mainly interested in the absoprtion process. From now on this model is adopted and we will refer to a molecule as a dipole, whose momentum is $\overrightarrow{d}_{exc}$, this dipole will interact with the local field and surrounding environment.

3.2   Photothermal deflection

Several detection techniques for the measurement of optical absorption and thermophysical properties are based on the change in refractive index in a medium, due to the interaction of the same with electromagnetic radiation. The absorbed energy is then converted in thermal energy. The list of these techniques includes thermal lensing, photoacoustic spectroscopy and photothermal deflection spectroscopy. The latter is the one that has been used in the present work. In order to give a physical description of this phenomena, imagine that there is an optically exciting beam which impinges on a given region of the sample. It might produce a number of different effects in the sample. Among them are the gain of the medium, absoption-induce temperature rise and thermal expansion, and change in refractive index. The contribution of each of these effects depend on the nature of the material and on the characteristics of the pump beam. In the picture we adopted to de-

scribe our method, the absorption of the radiation from the external pump beam causes a local temperature rise. The consequent thermal expansion of the medium produces a local change in the refractive index of the same. As the heat propagates a gradient of refractive index is produced in a thin layer adjacent to the sample surface. The thickness of this layer is dependent on the frequency of the pump beam and the characteristics of the adjacent medium. In particular an important parameter is the thermal length:

$$L_{th} = \sqrt{\frac{D}{\omega}}, \tag{3.2}$$

where ω is the frequency of the exciting laser and $D = \sqrt{\frac{K}{\rho C_p}}$. In the latter K is the thermal conductivity of the medium, C_p its specific heat and ρ its density. A second beam (probe beam) passes through this region and is deflected due to the refractive index change. The deflection can then be related to the optical absorption of the sample. Depending on the direction of the probe beam compared to the exciting beam, one can distinguish between collinear photothermal deflection,where the probe beam detects the refractive index change inside the sample, where the absorption itself happens, and transverse photothermal deflection (*mirage effect*), where the probe beam detects the refractive index change in a thin layer adjacent the sample surface. We are here interested in transverse photothermal deflection. The probe beam has a different direction then the exciting beam and doesn't travel in the sample region. The index of refraction of a material is a function of temperature and pressure. The pressure contribution (acoustic compression) can be neglected in this context. Hence one can write:

$$n(\overrightarrow{r}, t) = n_0 + \Delta n(\overrightarrow{r}, t) = n_0 + \frac{\partial n}{\partial T}|_{Tambient} T(\overrightarrow{r}, t), \tag{3.3}$$

where $\partial n/\partial T$ is in general $10^{-4\circ}C^{-1}$ for liquids and $10^{-5\circ}C^{-1}$ for solids. Solving the equation for a gaussian beam propagating in a region with varying refractive index, one gets that the effect of the gradient of refractive index

caused by the absorption is equivalent of having an astigmatic lens of focal length F_i in the S_i direction

$$\frac{1}{F_i} = -\frac{1}{n_0} \int_{path} \frac{\partial^2 n}{\partial S_{i\perp}^2} ds = -\frac{1}{n_0} \frac{\partial n}{\partial T} \int_{path} \frac{\partial^2 T}{\partial S_{i\perp}^2} ds \qquad (3.4)$$

$i = 1, 2$ With these assumptions the calculation of the propagation of the probe beam can be carried out. In the case when the thermal diffusion length of the medium is much smaller than the Gaussian pump-beam radius (that means a relatively low conductive medium, as it is in our case)

$$\phi = \frac{dn}{dT} \frac{T}{\omega \rho c \pi^2 a^2} \left[1 - e^{-\alpha l} \right] \left[-2 \frac{x_0}{a^2} e^{-\frac{x_0^2}{a^2}} \right] \qquad (3.5)$$

here dn/dT indicates the temperature coefficient of the index of refraction of the medium; P the power of the incident laser; ω stands for the angular modulation frequency of the pump beam; ρc is the heat capacity per unit volume of the medium; a indicates the radius of the pump beam at $1/e$ intensity and x_0 the offset between intensity maxima of the two beams; α is optical absorption coefficient and finally l the path length in the absorbing medium.

As already pointed out in CITATION!!! for small αl the deflection amplitude is directly proportional to the power of the exciting laser and inversely proportional to the modulation frequency. The optimum separation between the two beams can also be derived, in fact the deflection has a maximum at $x_0/a \sim 1$.

Chapter 4

Experimental

4.1 Introduction

In this chapter the experimental procedures are described.

In the first section we deal with the techniques used for the preparation of the samples. In the SPR a metal layer is needed, we used the electron beam evaporation technique to prepare them. The SPR experiment then was meant to verify the sensitivity of sol-gel deposited films in gas sensing. A brief description of this deposition technique is reported. As long as the near field topic is concerned, the layer-by-layer deposition of polyelectrolytes is described, together with their functionalization with chromophores molecules.

In the second section the principles of working of a UV-vis spectrometer are presented. This instrument has been used in the chromophores experiment for a first characterization of the films.

In the third section the experimental approach and set-up for the surface plasmon resonance experiment are described. In the forth section the attention is drown to two different experimental approach adopted for the chromophores experiment.

4.2   Sample preparation

4.2.1   Metal films

Electron Beam Physical Vapor Deposition (EBPVD) [6, 38] has been used for the preparation of the metal films which are necessary in the SPR experiments. EBPVD is a particular technique of physical vapor deposition. A point of reference for this technique is the work done by Graper E. [21, 22, 23, 24], who investigated the deposition characteristics of many materials. In evaporation the substrate is placed inside a vacuum chamber, in which an ingot (source) of the material to be deposited is also located. The source material is then heated to the point where it starts to boil and evaporate. The vacuum is required to allow the molecules to evaporate freely in the chamber, and they subsequently condense on all surfaces. This principle is the same for all evaporation technologies, only the method used to the heat (evaporate) the source material differs. There are two popular evaporation technologies, which are e-beam evaporation (the one we used) and resistive evaporation each referring to the heating method. In e-beam evaporation, an electron beam is aimed at the source material causing local heating and evaporation. In resistive evaporation, a tungsten boat, containing the source material, is heated electrically with a high current to make the material evaporate. Many materials are restrictive in terms of what evaporation method can be used (i.e. aluminum is quite difficult to evaporate using resistive heating), which typically relates to the phase transition properties of that material. In figure 4.1 a picture of a typical system used for evaporation of materials is shown. The evaporation rate is dependent on many factors relating the environment conditions in the chamber and the characteristics of the material to be deposited. From now on $P_e(T)$ indicates the equilibrium vapor pressure of the evaporant at T and P the ambient hydrostatic pressure acting upon the evaporant in the condensed phase. Heinrich Hertz found experimentally that the
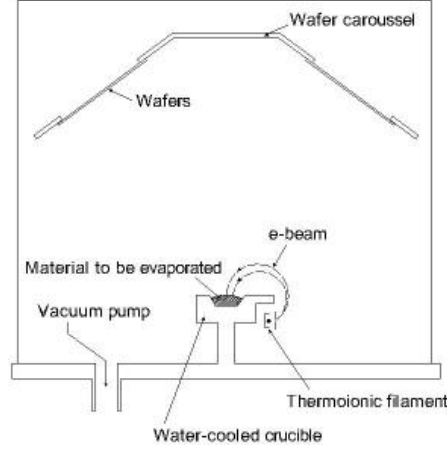
Figure 4.1: Typical system for e-beam evaporation of materials.

evaporation rate was proportional to $(P_e(T) - P)$. This is consistent with kinetic theory in which the impingement rates are proportional to pressure. Hertz also found that the evaporation rate could not be increased by supplying more heat unless the equilibrium vapor pressure was also increased by this action. Thus,there is a maximum evaporation rate set by $P_e(T)$, and this is only achieved in a vacuum, where P = 0. Knudsen postulated that the evaporant vapor molecules impinging upon the condensed phase surface may be reflected back. A sticking coefficient has to be taken into consideration. The rate of deposition is well expressed by the "Hertz-Knudsen law", reported in equation 4.1. In this equation all the previous assumptions and results are included.

$$R_m = C_m \left(\frac{M}{T} \right) cos\theta cos\varphi \frac{1}{r^2} \left(P_e(T) - P \right) \tag{4.1}$$

C_m is a dimensionless constant; M the atomic weight of the evaporant; T the absolute temperature; θ the angle with the normal to the material ingot; φ the angle with the local normal to the condensation surface.

The facility available at the LUXOR-INFM laboratories resembles the just described one. The vacuum chamber has a cylindrical shape (ISO 400) and it's made in stainless 304 steel. Two kind of vacuum pumps are used

in combination: a turbomolecolar pump and a cryogenic pump. In this way it can be reached a pressure of less than $2 \cdot 10^{-7}$ bar, but if a titanium evaporation in the chamber walls is performed the reachable vacuum downs to $8 \cdot 10^{-8}$. The residual pressure is due to some gases still present on the chamber. These are monitored by a quadrupole, which shows that they are mainly water, carbon monoxide, nitrogen and ammonia. A TEMESCAL e-beam gun, which can mount four crucibles, is used for deposition. The substrate holder is flat and can be rotated. A picture of it is shown in the picture 4.2.

It is a vacuum deposition technique. A charged tungsten filament is used as

Figure 4.2: Picture of the EBD facility at LUXOR laboratories

a source of electrons. The electron beam is then directed to a target anode, in this way atoms from the target evaporates and eventually precipitate into

solid form, producing a thin layer of the anode material on everything in the vacuum chamber. The samples are placed with proper holders on a rotating plate in top of the chamber. This plate rotates during the deposition to assure uniform deposition conditions for the different samples. A quartz balance is inserted in the vacuum chamber in order to control *in situ* the thickness of the layer being deposited.

The material to be deposited is in the form of small ingots. The electron beam is generated by thermionic emission by a tungsten filament and it's accelerated to hight kinetic energy and focused through the application of magnetic lenses on the target. The source of electrons is placed at 270° with respect to the material. The electrons flux goes to affect the material to be deposited which is located in a water cooled crucible. Over threshold conditions of voltage (20 - 25 kV) and current (few amperes), the kinetic energy of the electrons is converted into thermal energy as the beam impinges onto the ingots, in this way a liquid melt is produced on the surface. This liquid then evaporates under vacuum. It's only in this moment that the shutter over the ingots has to be open and the deposition starts. The rate of deposition and the thickness is controlled by a microbalance inside the chamber. In our facility we have a quartz balance.

Vibrating Quartz Method The main part consists in a accurately cut and polished quartz plate with electrodes deposited on opposite sides. The evaporating material deposit on one electrode which is connected to an oscillating circuit. The crystal of thickness t has a fundamental resonance frequency $f = v_p/2t = N/t$, where v_p is the velocity of transverse elastic waves in the direction of the thickness t, and N is the frequency constant. The frequency, f, is dependent from the mass, m, the latter can be related to the thickness knowing the density of the material, ρ_k.

$$dt = \frac{1}{\rho_k S} dm$$
$$\Downarrow$$
$$df = -\frac{f^2}{N \cdot \rho_k} \cdot \frac{dm}{S}$$

(4.2)

From the relations in eq. (4.2) can be understood how the thickness can be derived from a detection of frequency change.

4.2.2 Sol-gel technique

There is already a wide part of literature pointing out the important role of nanostructured semiconductors metal oxides, as titanium dioxide, in sensing. In the works of Manera, Fernandez*et al.* [12, 15]it has been pointed out the capability of these substrate in vapor organic compounds sensing. This feature is due to the chemical disorder and high porosity of these materials. The characteristics depends on the synthesis method and parameters. To enhance the sensing properties of these materials metal nanoparticles can be dispersed in them. They act in two ways, on one side they increase the contact surface between the film and the gas to be sensed and on the other side optical sensing is enhanced by a localized surface plasmon resonance at the nanoparticles.

The TiO_2 sol has been prepared using titanium isopropoxide (Ti), isopropanol (IPA) and acetic acid (AcOH) with a molar ratio Ti : AcOH : IPA = 1 : 6 : 1.3. In order to synthesize the Au-TiO2 nanocomposite films, a colloidal solution containing Au spherical nanoparticles has been prepared and afterwards mixed with the previous described sol. A seed-mediated growth method was used to obtain the solution that consists of spherical nanoparticles that are stabilized by poly(N-vinylpyrrolidone) and dispersed in ethanol. The gold solution and TiO2 sol were mixed with a percentage such that the Au/Ti ratio was 2%. The sol has been deposited by standard spin-coating on the SPR substrate, which consisted of a thin metal film deposited on a glass slide.

The spin rate used was 5000 r.p.m. The film were then annealed at 200°C during 10 minutes in air. The first characterization has been performed using a profilometer (Alpha Step 200 Tencor Instrument) on the step made by scratching the film after the deposition. For the thin film parameters see tables in chapter 5. TiO2 and Au-TiO2 thin film thickness was measured.

4.2.3 Polyelectrolyte with dyes

Fluorescent organic dyes can be used as molecular probes of local electromagnetic fields. Moreover if these are coupled to polymers, they constitute a good system in terms of costs effectiveness, sample preparation and flexibility. The key point is that adsorption of polyelectrolytes can be controlled well down to a thickness of a few nanometers using the layer-by-layer technique, this enable us to control the position and the environment of the molecular probes.

Substrate preparation As support for the polyelectrolytes BK7 slides have been used. They are both sides optically polished and with dimensions 26mm x 76mm x1.1mm (PGO GmbH).They were cleaned with a 2% solution detergent (Hellmanex -Hellma GmbH) in an ultrasound bath for 15 minutes and rinsed with ultrapure water twice (MilliQresistivity, $18.2Mcm$). After successive rinsing with ethanol (Fischer Scientific), the slides were dried by a N2 flow and successively immersed in a bath of $H_2O_2 : NH_3 : H_2O$ (10ml : 10ml : 50ml). There, NH_3 solution 32% and H2O2 solution 34% have been used. The slides were left in the solution for 45 minutes at $80°C$. After rinsing 20 times with ultrapure H_2O and ethanol, the slides were carefully dried by a N_2 flow and put in a closed flask with 0.5ml (3-Aminopropyl)-triethoxysilane (3-APTES, CAS: 919-30-2, Sigma Aldrich Inc.). The closed flask was then put in a oven, under vacuum, at 130°C for 3 hours [57]. After cooling down the slides were rinsed two times with ethanol to remove physisorbed silane

aggregates from the surface and rinsed additionally 20 times with ultrapure water. At the end, the substrates were dried by N_2 and used as first charged layer for deposition of polyelectrolytes.

Polyelectrolytes deposition   The silane provides a quite uniform positive charge onto the slide surface. In order to guarantee a more uniformly charged surface 2 bilayers PSS-PAH [poly(styrene sulfonate) / poly(allylamine hydrochloride)] and a PSS layer have been deposited. The PSS solution components are:

- 50mL of ultrapure water (resistivity of 18.2Mcm)

- 4.049g of MnCl2 salt (Alfa Aesar)

- 0.207g of PSS (CAS: 25704-18-1, Mw #70000, Sigma Aldrich)

- 0.5mL of HCl 0.1N was added to adjust the pH to 3

The PAH solution components are:

- 50mL of ultrapure water (resistivity of 18.2Mcm)

- 10.29g of NaBr (Alfa Aesar)

- 0.0935g of PAH (CAS:71550?12?4, Mw #15000, Sigma Aldrich)

- 0.5mL of HCl 0.1N was added to adjust the pH to 3

The low pH value guarantees that the PAH chains are fully ionized [14]. The BK7 slides were immersed in the two solutions alternatively, each time for 20 minutes to guarantee the adsorption of the polyeletrolytes on the surface. After each immersion the samples were rinsed 10 times with ultrapure water. When the desired number of deposition cycles had been reached, the slides were dried with a N2 flow and stored under room conditions.

PAH functionalization   The fluorescent molecular probe had to be bound to the PAH. The condensation reaction used is shown in figure 4.3. As an example for the dye Atto633 NHS ester (Sigma Aldrich Inc.) the procedure followed has been the following. The first step consist in dissolving 24.5 mg of PAH ($2.63 10^{-4}$mol) in 5 ml of bicarbonate buffer (NaHCO3,50mM,pH $=$ 9.0). To this solution 50?l fluorescent red dye in DMF was added ($5 10^{-5}$mol). The solution was incubated in the dark for one hour.
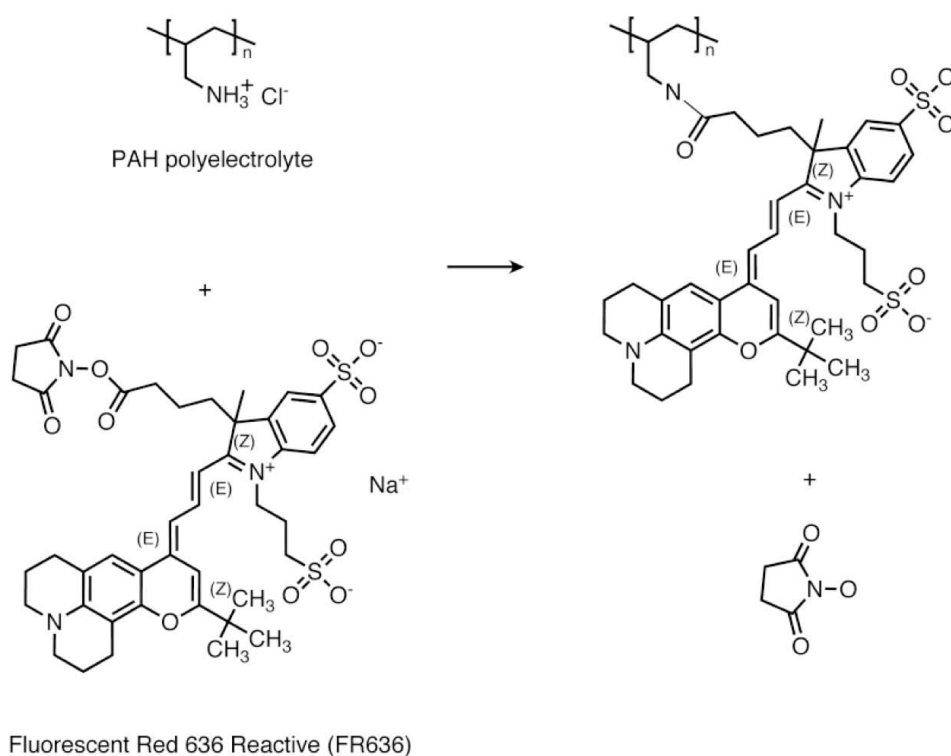

Figure 4.3: Scheme of functionalization of PAH with Fluorescent Red 636 reactive dye

The Atto-functionalized PAH was then purified by adding acetone (200ml) to precipitate the polymer and the solution was filtered to collect the functionalized polymer as powder. After drying through a vacuum pump, the

functionalized PAH can be stored in dark at ambient conditions. The so-
lution has been then prepared and used for deposition as described in the
previous paragraph. As already pointed out, the layer-by-layer technique
permits to control the distance of the chromophores from the interface with
an accuracy of a few nanometers. Ascheme of how a sample is structured
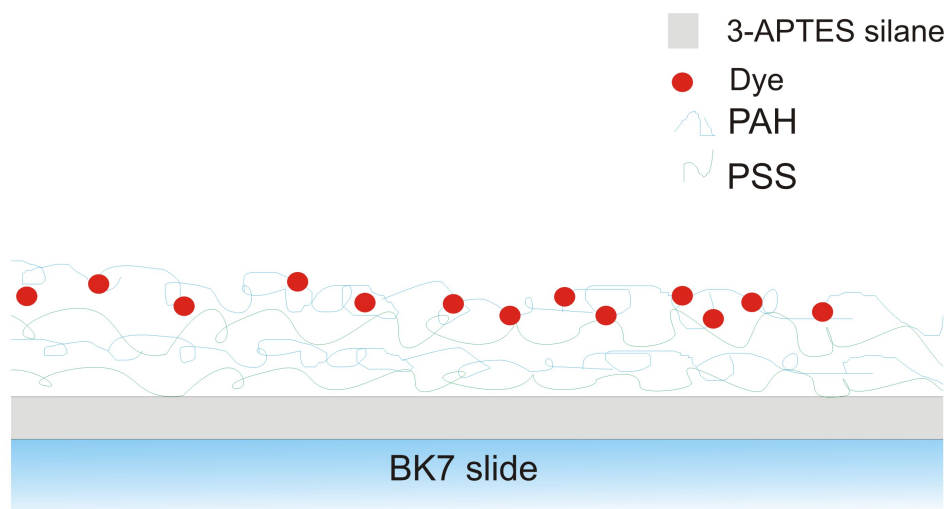after the deposition is shown in figure 4.4.

Figure 4.4: Scheme of samples for in-polymer case

4.3   Sample characterization

4.3.1   UV-vis spectroscopy

The polyelectrolytes samples were first charachterized with a UV-vis spec-
trometer (Perkin Elmer, UV/VIS/NIR spectrometer, Lambda900), in order
to get the absorption spectrum in the region 400-800 nm and a first estimate
of the amount of fluorescent molecules present on the sample under investi-
gation. Ultraviolet and visible (UV-Vis) absorption spectroscopy indicates
in general the measurement of the attenuation of a beam of light after it

passes through a sample or after reflection from a sample surface. Absorption measurements can be at a single wavelength or over an extended spectral range. Ultraviolet and visible light are energetic enough to promote outer electrons to higher energy levels, and UV-Vis spectroscopy is usually applied to molecules or inorganic complexes in solution. The UV-Vis spectra have broad features that are of limited use for sample identification but are very useful for quantitative measurements. The concentration of an analyte in solution can be determined by measuring the absorbance at some wavelength and applying the Beer-Lambert Law, $A = -\log \frac{I}{I_0}$, where I_0 is the incident light intensity, A is the absorbance .

There are two kinds of UV-vis spectrometer. The type that we used is called a scanning spectrophotometer because it measures the intensity of transmitted light of a narrow bandpass, and scans the wavelength in time in order to collect a spectrum. Since absorption is a ratio-metric measurement, these instruments generally require the user to measure two spectra, one sample and one blank. The blank should be identical to the sample in every way except that the absorbing species of interest is not present. This can be done either consecutively with a single beam instrument followed by the ratio calculation, or simultaneously with a dual beam instrument. The dual beam method is faster, and has the added advantage that lamp drift and other slow intensity fluctuations are properly accounted for in the ratio calculation. Collecting spectra with scanning spectrophotometers is slow, but the instruments often have very high resolving power owing to the use of photomultiplier tube detectors, which can be used with very narrow slit widths.

The second configuration employs a photodiode array. This is a 1 or 2 dimensional stack of individual photodiode detectors, each of which makes an independent measurement of the incident light intensity at its particular

location. One dimensional arrays are often used in spectroscopic instrumentation. If the array is placed at the focal plane of a monochromator, then the position of each photodiode will be associated with a specific bandwidth of light. Thus the maximum resolution of the instrument is limited by geometric issues and the number of diodes available, typically it is of ∼1 nm. This is not as good as the typical resolution of a scanning instrument (resolutions of about 0.2 nm are not uncommon with scanning instruments), but for many applications (especially molecular solution spectroscopy where absorption bands are typically very broad) 1 nm is adequate. The real advantage of the instrument is its speed. A single spectrum can be taken in about 0.1 seconds.
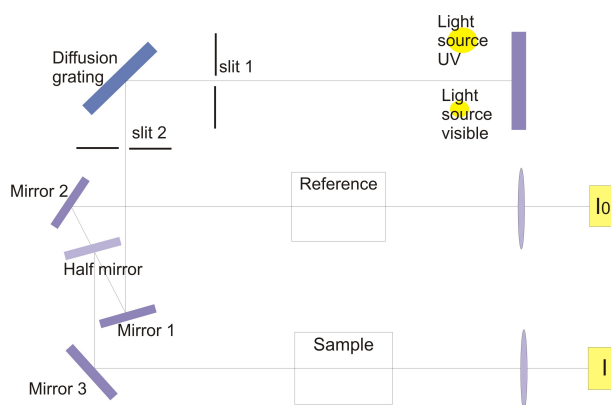

Figure 4.5: Scheme of main components of a scanning spectrometer

Measurements have been performed with a scanning spectrometer. The light source is a deuterium discharge lamp for UV measurements and a tungsten-halogen lamp for visible and NIR measurements. The instrument automatically swaps lamps when scanning between the UV and visible regions. The wavelengths of these continuous light sources are dispersed by a holographic grating in a single or double monochromator or spectrograph. The spectral bandpass is then determined by the monochromator slit width

or by the array-element width in array-detector spectrometers. Spectrometer designs and optical components are optimized to reject stray light, which is one of the limiting factors in quantitative absorbance measurements. The detector in single-detector instruments is a photodiode.

4.4 SPR

The Surface Plasmon Spectrometer has been design following the Kretschmann geometry, hence the principal components are a light source, a prism of dielectric material on a rotation stage and coupled to a metal layer, a detector on a movable arm. The main issues followed have been easy handling, noise reduction and flexibility.

4.4.1 Set-up build-up

Optical bench set-up   Our experimental set-up mainly consists of:

- Light sources:

    - He-Ne laser, $\lambda = 632.8nm$;

    - Red LED L6108 Hamamatsu (peak emission wavelength: 670 nm; Spectral half width: 25 nm);

    - Red Diode Laser, $\lambda = 635nm$;

    - Green Laser Imatronic, $\lambda = 532nm$;

- Objective and collimation lenses;

- Dichroic polarizer (Extinction ratio: 1×10^{-4} ; Transmittance @550nm: 0.36);

- Rectangular prism (side length: 25mm, BK7);

- Schott glass buffer (Boroflat 33);

- Detector: photo-diode Thorlabs (400-1100nm);

4.4.2   Set-up handling

Spatial filter   In the measurements where the He-Ne laser has to be used, it was necessary to "clean up" the beam through a spatial filter. A laser system usually does not produce a beam with a smooth intensity profile. In order to produce an approximate clean Gaussian beam, a spatial filter is used to remove the unwanted multiple-order energy peaks and pass only the central maximum of the diffraction pattern (see illustration 4.6). Also dust in the air or on optical components can disrupt the beam and create scattered light. This scattered light can leave unwanted ring patterns in the beam profile. The spatial filter removes this additional spatial noise from the system. The spatial filter consists of an objective lens, a pinhole aperture, and an image lens to collimate the beam with the desired diameter. The pinhole is mounted on a positioning mechanism with precision $x - y$ movements to be centered at the focal point of the objective lens. A proper pinhole and objective combination has to be chosen in order to get optimal results.

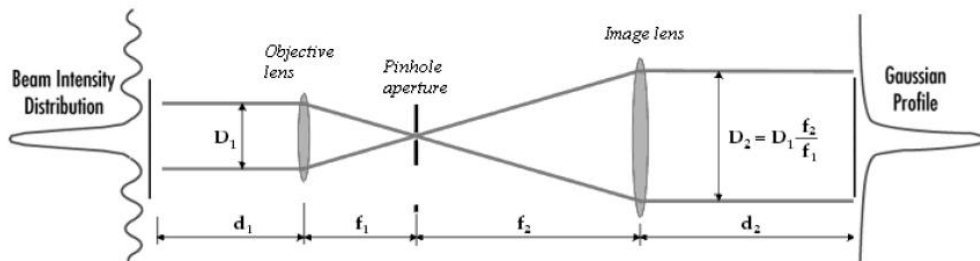The following equations were used to select the proper pinhole aperture:

Figure 4.6: Schematic layout of the spatial filter assembly.

$$D_{BS} = \frac{1.27 \cdot \lambda \cdot f_1}{D_1} \qquad (4.3)$$

$$D_{ph} = 1.5 \cdot D_{BS} \qquad (4.4)$$

In the previous relations D_{BS} stands for beam spot diameter; D_1 the input beam diameter; f_1 is the focal length of objective lens and D_{ph} is the pinhole diameter.

Since the beam waist of our He-Ne laser is about 408 μm, the pinhole diameter should be 195 μm. So a 200 μm pinhole has been chosen.

Once the pinhole diameter has been set, one can define the proper focal length and position of the image lens from the knowledge of the divergence of the beam. The pinhole is circular, so it can be assumed as a point source. The divergence of the central spot of the outgoing beam is given by $2.44 / D_{ph}$, but for intensity evaluation $1.22 / D_{ph}$ is more useful, since most of the energy (70%) is contained within that cone-angle.

In order to verify the collimation of the beam and if only the TEM00 mode was selected, a beam profiler has been used. It is basically a CCD camera of 1024×768 pixel.

In the graphs in figure 4.7 the beam section of the beam just after the polarizer and far from it about $50cm$ are presented. The straight line indicate the height at which the beam waist has to be calculated. It is estimated through the intersection of this line and the Gaussian fit of the experimental profile.

LED broad bandwidth The same principle has been used to filter the LED source, since LED usually have not a uniform illumination, in particular they have different divergences in the vertical and horizontal plane. So through focusing it in a pinhole, a point-like source has been created. The second lens is used to collimate the beam. An additional iris is introduced
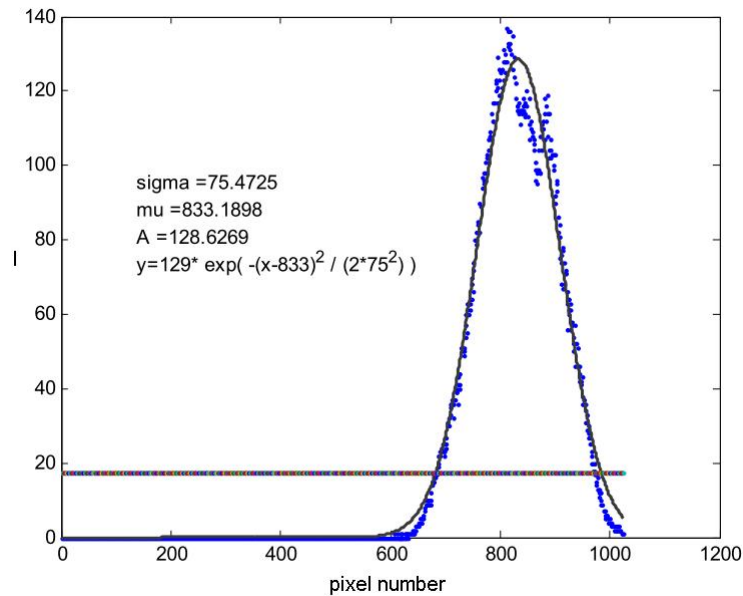
Figure 4.7: Beam profile and relative gaussian fit of the beam just after the polarizer.

downstream in order to limit the diameter size of the beam. The pinhole diameter in this case has to be larger because otherwise too much intensity gets lost.

 Another drawback of using the LED source is that it is not monochromatic. As can be seen in the following graph, its spectrum has a Gaussian shape centered at the nominal wavelength.

 In order to estimate what the effect of such a finite bandwidth could be on the measurements, I summed different wavelengths contributions with the appropriate weights, as can be seen in figure 4.11. It is worth to note that in this calculation I assumed the literature values for the optical constants of metals, in this way they are available for each wavelength considered.

 From figure 4.12 it is evident that the effect of the finite bandwidth of the light source is an higher reflectivity in corrispondence of the minimum of
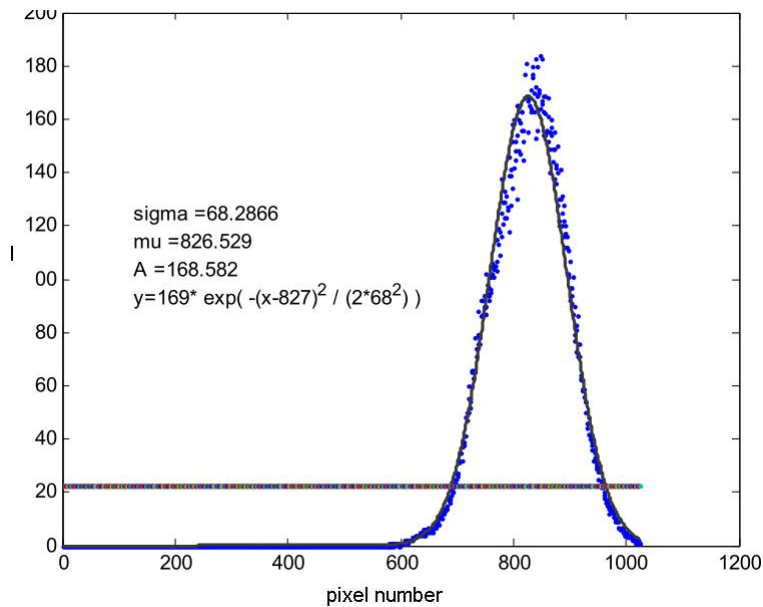
sigma =68.2866
mu =826.529
A =168.582
$y = 169 \ast \exp(-(x-827)^2 / (2 \ast 68^2))$

pixel number

Figure 4.8: Beam profile and relative gaussian fit of the beam at 50 cm from the first profile caption.

the resonance curve.

4.5 Chromophores absorbance - photothermal deflection

4.5.1 Introduction

In the following section the experimental steps followed in the chromophores absorption measurement are explained. Two experimental approaches are described. The first is based on a fast modulating angle technique, while the second employ the so called "mirage effect", based on a change of refractive index induced by the absorption. Both the methods use a lock-in demodulation technique to improve the signal to noise ratio.
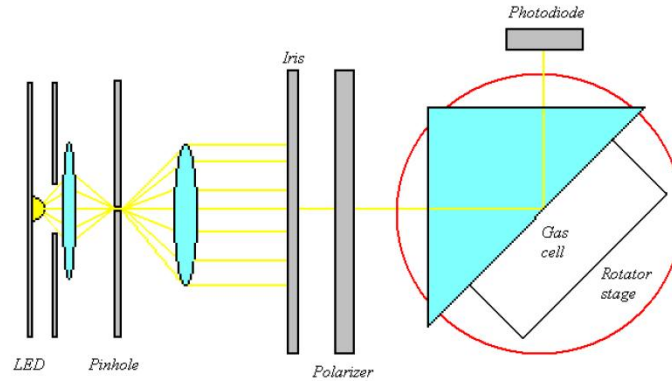
Figure 4.9: Schematic layout of the experimental set-up with LED source. While using He-Ne laser some neutral filters have to be added. When instead using diode laser the spatial filter assembly is removed.

4.5.2   Fast modulating angle approach

The physical phenomena we're expecting to detect is very weak so while thinking of an experimental set-up capable to reveal this signal, the main issues are sensitivity and very high signal to noise ratio. The first idea which has been tempted consisted in modulating with a high frequency ω the angle of incidence θ near the TIR edge. If nothing absorbs the evanescent field, no changes in reflectivity should be detected. If some chromophores interact with the local field, we expect a decrease in the reflected power, this produces a signal in the lock- in demodulated signal, since the lock-in reference signal has the same frequency of the angle modulation. The idea is illustrated in figure 4.13

 Mathematically this can be understood as:

$$\theta = \theta_0 + \Delta\theta \sin(\omega t)$$
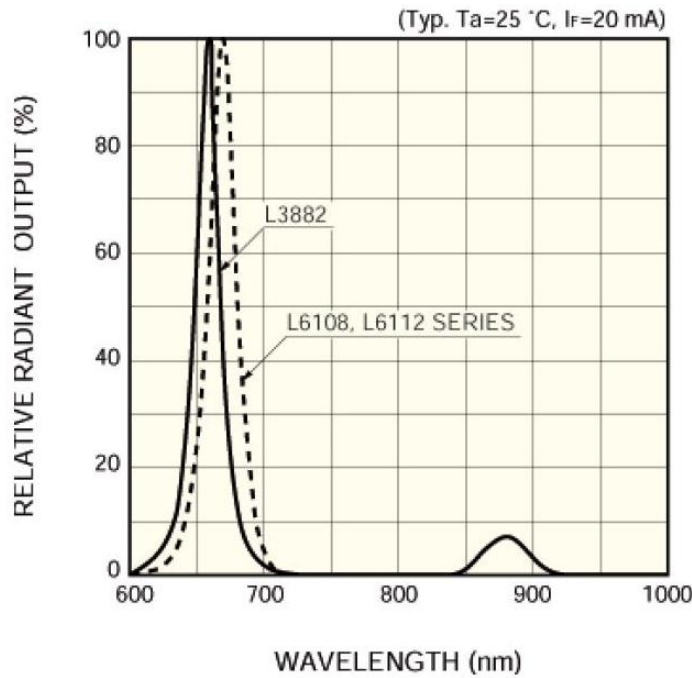
$$\Downarrow$$

Figure 4.10: LED relative radiant output as a function of wavelength. The one used in our tests is the L6108. (Figure from Hamamatsu datasheet)

$$I = I_0 \sin(\omega t)$$

The main experimental component to accomplish this task was a piezoelectric stage that could move in a direction of ± 100 μm. On this stage a mirror has been mounted to deviate the collimated light beam. The beam passes through a lens which bend the beam at different angles, depending on the distance from the optical axis at which the beam impinges onto the lens. In order to have a satisfying optical bending a short focal lens has been adopted, precisely the focal length is $f = 50$ mm. The focus of the "bending lens" coincides with the back of an hemicylindrical prism. These parameters create a constraint in the accessible range of angles, as can be seen in the following
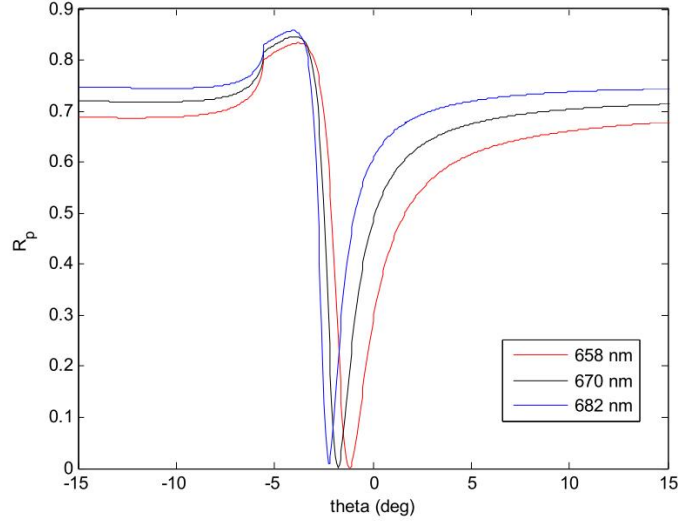
Figure 4.11: Theoretical SPR curve for three different wavelengths.

derivation (4.10):

$$\Delta h = 0.1mm$$
$$\Downarrow \qquad\qquad\qquad , \qquad\qquad (4.5)$$
$$\Delta\theta = \frac{\Delta h}{f} = \frac{0.1}{50}rad = 2 \cdot 10^{-3}rad = 0.1°$$

We chose a prism of cylindrical shape because in this way the rays impinges perpendicularly to the prism surface and are not bended by it. A schematic layout of how the set-up looks like is shown in figure 4.14

A second lens has been inserted after the prism stage. Its focus coincides with the detector plane, in this way different rays coming from different heights impinge onto the detector (which is not moving) in the same point. First experimental tests concerned the verification of the sensibility of the set-up to the movements of the piezo-stage. So an agular spectra has been recorded (figure 4.15). Then we set the angle at the point of maximum slope, $\theta = 42.2°$, turned on the piezo stage and recorded the signal at the detector as a function of time (figure 4.16).

The detected signal show a periodic behavior compatible with the input sig-
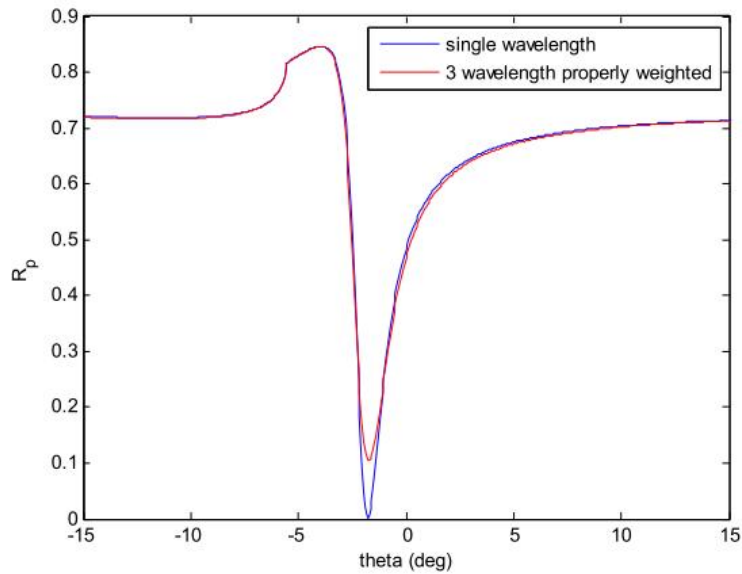
Figure 4.12: The blue line represent the SPR curve, calculated for a single wavelength (670nm). The red line label the SPR curve obtained through the weighted sum of the three curves of the previous figure.

nal, so it seems that the system is sensitive to the piezo-movement. As can be seen from figure 4.15 the curve presents some "wobbling" around the angle of 45°. This feature represents itself in the same shape when the measure is repeated. On the other hand it is something that we don't expect from calculations. It is due to internal reflections in the prisms at this particular angle. In order to avoid this problem and to get a flat response in the TIR region, a lens with long focal length has been inserted before the prism stage. The solution is graphically explained in figure 4.17 and the results after this solutions are shown in figure 4.18 and figure 4.19, where the level noise is pointed out.

In this last figure two consecutive scan measurements are shown together. The fact that no reproducible feature are evident, proves that the sources of systematic errors have been cancelled. The noise which can be seen is ran-
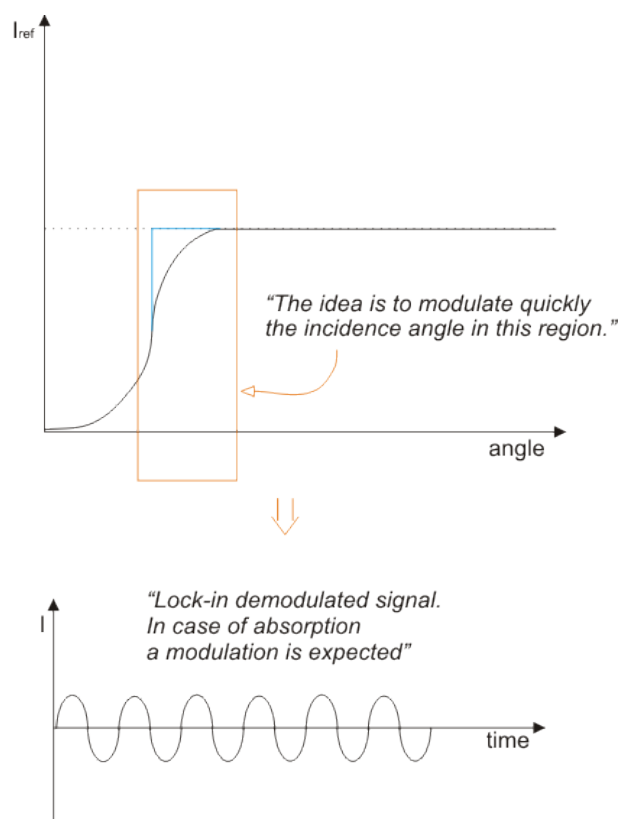
Figure 4.13: Description of the first experimental approach. If the reflected intensity varies in the range of angles spanned by the incidence angle, a signal is detected

dom noise and its level is of a good order of magnitude ($\sim 0.1\%$). So finally I prepared some samples with a Atto-633 loaded PAH. In figure 4.20 the response between a clean sample and one with dyes deposited on it is shown. In figure 4.21 the theoretical response expected for the same system is shown.

The experimental tests show that the absorption actually takes place, so in principle we can detect the interaction between the local field and the chromophores. By the way the modulation is not enough for the angle modulation approach. For this reason it has been necessary to look for a second experimental solution. It's described in the following paragraphs.
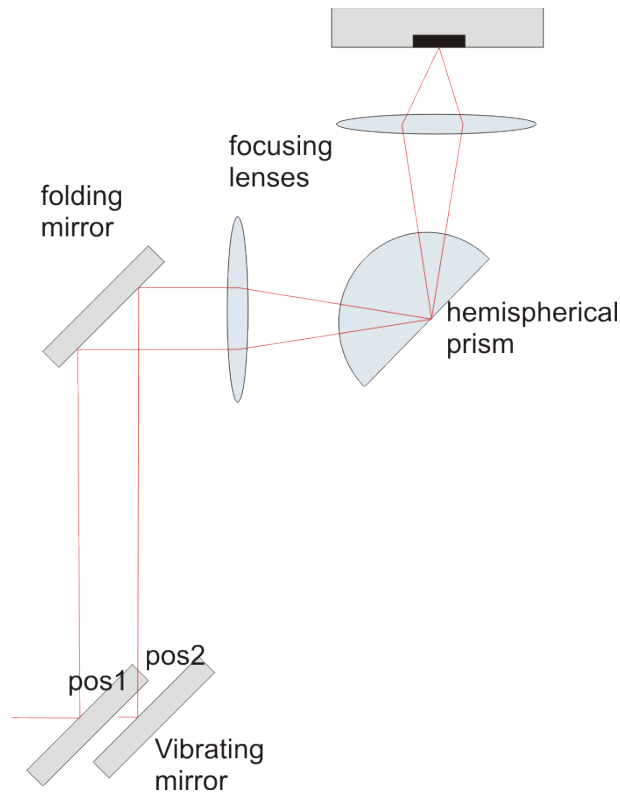
Figure 4.14: Schematic layout of the first experimental setup. The principal optical components are shown

4.5.3 Set-up PTD

In this paragraph the set-up used in the photo-thermal approach is presented in details. The set-up has been built as if it were a Kretschmann set-up for the detection of Surface Plasmon Resonance. This means that essentially it's consistent in a light source, a polarizer, a prism and a detector. Some other components has then been inserted to suit the set-up to our purposes. The set-up has been built on an optical breadboard; the sample holder and the detector have been placed within a metal black-box, to reduce the background. The area containing the laser source and the required optics for chromophores excitation have been placed externally the black-box. A system of flipping mirrors and two laser supports were also installed for an
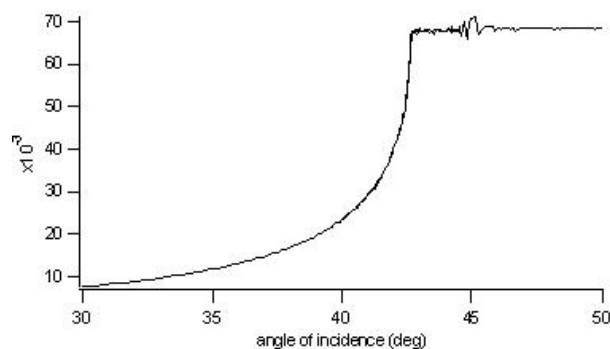
Figure 4.15: Reflectivity as a function of the incident angle for a BK7 prism
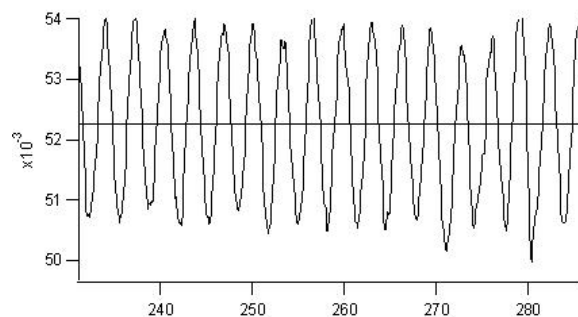

Figure 4.16: Reflectivity as a function of time is reported, while modulating the angle of incidence in a little range around $42.2°$.

easy optical alignment of the excitation and the detection devices. The set-up can switch between two wavelengths. It is provided with a He-Ne laser ($632.8 \ nm$) and a laser-diode green laser ($532 \ nm$) in order to be used with different kinds of dyes molecules, with the excitation band comprising this range. The light sources are placed outside the black-box. In both paths a system of folding mirrors directs the beam to the sample. For each beam a couple of polarizers and iris are placed. The firsts are needed to regulate the intensity and the polarization of the beam. The iris pinholes are useful for a fast alignment of the beam. In the black-box there are the sample holder and the optics for the probe beam, as described in figure 4.22. The probe
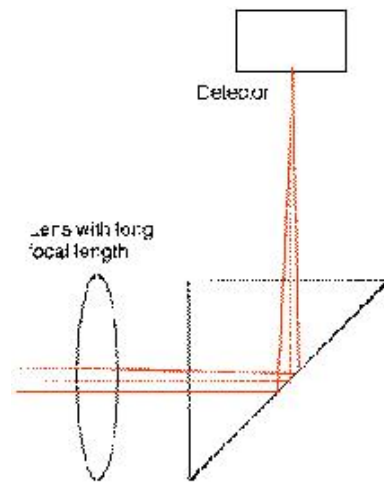
Figure 4.17: Set-up adopted to improve the flatness of the TIR region. A lens with long focal length focus the beam on the detector, so the rays are not perpendicular to the faces of the prism, and the wobbling noise is avoided.

beam is also a He-Ne laser. On a rail which rotates together with the sample holder the following optical components are mounted:

1. Laser He-Ne;

2. Folding mirrors, to direct the beam through the glass slide;

3. Optical filter, to reduce the beam intensity;

4. Focusing lens, to focus the beam into the glass slide;

5. Position detector.

4.5.4 Photothermal deflection

Position sensor In figure 4.24 the experimental configuration is shown. To detect the deflection of the probe beam a lateral position sensor has been
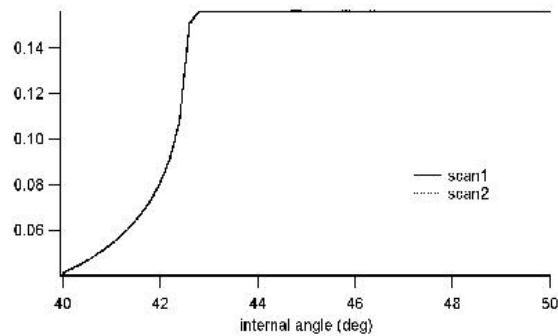
Figure 4.18: Reflectivity as a function of incidence angle after lens insertion
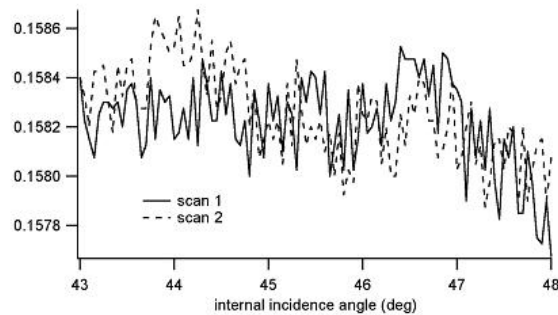
Figure 4.19: Reflectivity as a function of incidence angle. Two consecutive measurements are shown. This proves that the features are due only to random noise.

used. This converts the deflection into an output voltage, this signal is sent to the differential input of a lock-in amplifier. For this kind of detectors the signal depends on the distance between the detector itself and the focal spot. If l is the lateral size of the detector

$$d_{max} = \frac{(l\pi w_0 n_0)}{\lambda} \tag{4.6}$$

Dual Phase Lock-In Amplifier Lock-In amplifiers are used to detect signals buried in noise. The technique used is called phase-sensitive detection, it isolates the component of the signal at a specific reference frequency and phase. Noise signals, at frequencies other than the reference frequency, are

Figure 4.20: Comparison of experimental results between a sample with and on without dyes
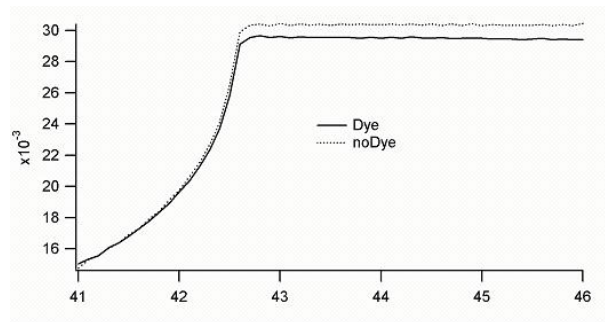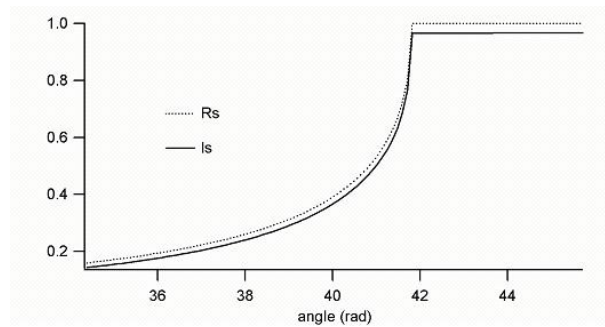

Figure 4.21: Theoretical calculation; Is is the expected intensity without absorption and Rs the expected reflectivity if light at the interface is absorbed.

rejected and do not affect the measurement. It's useful to have a deeper look at how this instrument works.

The experiment generally is excited at a fixed frequency (from an oscillator or function generator), and the lock-in detects the response from the experiment at the reference frequency. In the diagram in figure 4.23, the reference signal is a square wave at frequency ω_r. This is in the present set-up the sync output from the optical chopper, which modulates the exciting beam.

The detected signal is expected to have the same frequency modulation as the excitation, hence to be of the form $V_{sig} \sin(\omega_r t + \theta_{sig})$ where V_{sig} is the signal amplitude, ω_r is the signal frequency and θ_{sig} is the signal phase.
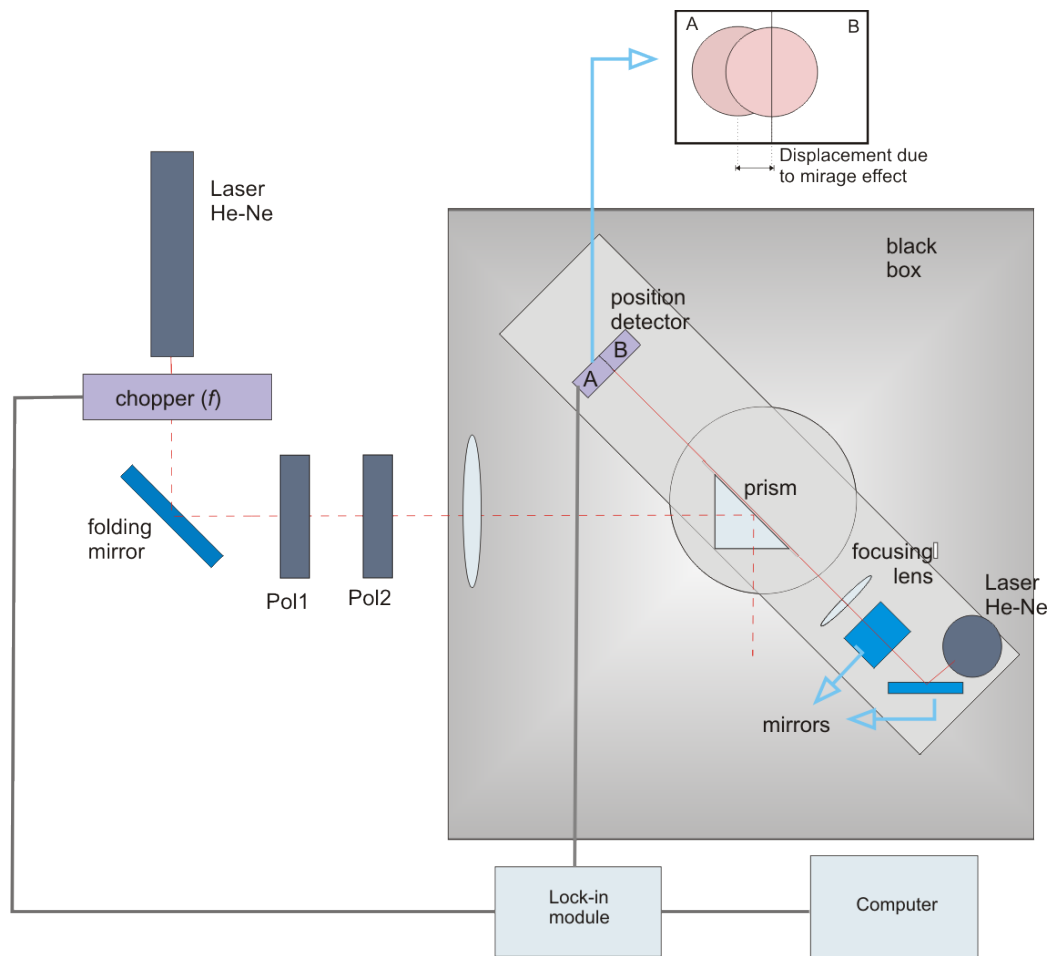
Figure 4.22: Cartoon of the experimental set-up. The position of the optical components is shown.

Lock-in amplifiers generate their own internal reference, as shown in figure 4.23. $V_L \sin(\omega_L t + \theta_L)$ The signal is then amplified and multiplied by the lock-in reference using a phase-sensitive detector (PSD). The output of the PSD is simply the product of two sine waves.

The PSD output is two alternate signals, one at the difference frequency $(\omega_r - \omega L)$ and the other at the sum frequency $(\omega_r + \omega L)$. If the PSD output is passed through a low pass filter, the AC signals are removed. But if

Figure 4.23: Relation between signals in a Lock-In amplifier. θ_{sig} is the phase difference between the signal and the external reference. θ_{ref} is the phase difference between the lock-in reference and the external reference.

$(\omega_r = \omega L)$ the difference frequency component will be a continuous signal, not filtered. Hence what remains of the signal would be:

$$V_{PSD} = \frac{1}{2} V_{sig} V_L \cos\left(\theta_{sig} - \theta_L\right) \tag{4.7}$$

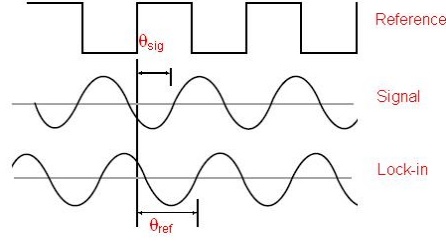In the case where $\theta_{sig} - \theta_L = 90°$, there will be no output at all. A lock-in with a single PSD is called a single-phase lock-in, the output has the form $V_{PSD2} = V_{sig} \sin\left(\theta_{sig} - \theta_L\right)$. This phase dependency can be eliminated by adding a second PSD. If the second PSD multiplies the signal with the reference oscillator shifted by 90°, its low pass filtered output will be:

If one calls the first output $X = V_{sig} \cos\theta$ and the second $Y = V_{sig} \sin\theta$, the magnitude of the signal can be computed and the phase dependence removed.

$$R = \left(X^2 + Y^2\right)^{1/2} = V_{sig} \tag{4.8}$$

A dual-phase lock-in has two PSDs with reference oscillators 90 apart, and can measure X, Y and R directly. Moreover the phase between the signals can also be derived as

$$\theta = \arctan\left(\frac{X}{Y}\right) \tag{4.9}$$

4.5.5 Set-up handling

In this second experimental approach we try to detect the very low signal due to the thermo-optic effect induced by the absorption, through a lock-in demodulation technique. In the figure 4.24 the basics of the set-up are shown. A first laser, whose wavelength matches the excitation wavelength of the choromophores in use, is chopped at a frequency f. It impinges form the inside onto the back side of a triangular prism. The angle is firstly set in order to be at the beginning of TIR (total internal reflection) region. This produces a local field that eventually interacts with the molecules on the back side of the prism, as describer in chapter 2. The latter interaction leads to a local increase of temperature, which causes a periodical (f) local change in the refractive index. A second He-Ne laser is focused in the long side of a thin (1.1 mm) BK7 slide matched at the back of the prism. This laser is periodically (f) deflected by the thermal lens due to the local refractive index change. The deflection is monitored through a beam position detector. This signal goes to a lock-in amplifier driven by the frequency of the chopper. In this way we can extract the signal at the same rate of the excitation from the noise.

The beam waist of a laser beam is the location along the propagation direction where the beam radius has a minimum and we want it to fall into the glass slide. A small beam waist can be obtained by focusing a laser beam with a lens which has a high numerical aperture, and making sure that the lens aperture is largely filled by the input beam. For this reason a lens of proper focal length and proper diameter has been chosen to wave the beam focused in the glass slide. The situation is explained in figure 4.24. The
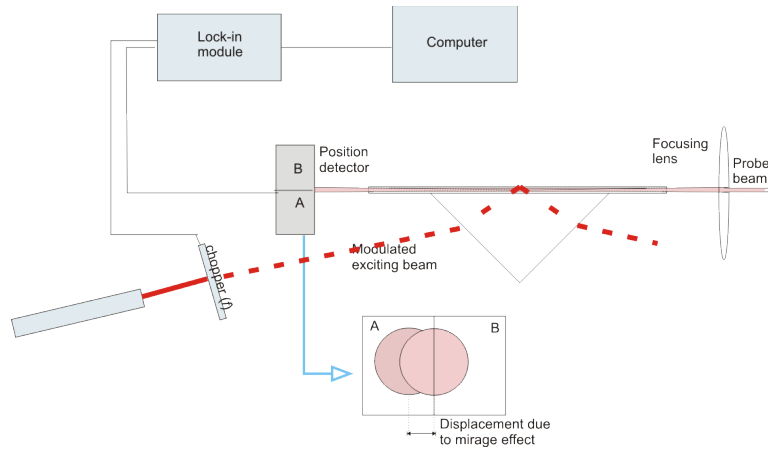
Figure 4.24: Schematic layout of the main components of the second approach experimental set-up

equations 4.10 clarify the calculation made to estimate the wanted parameters, once the thickness and length of the glass slide is known.

$$
\begin{aligned}
\theta &= \frac{\lambda}{\pi w_0} \\
\theta_0 &= \frac{h}{l} \\
\theta_0 &= \frac{w_s}{L} \\
L &= \frac{l}{h} w_s = 70 \ mm
\end{aligned}
\quad , \tag{4.10}
$$

The measure is very sensible to environment perturbations, like vibrations. For this reason particular attention has been paid in making the system the more stable as possible. One important point in adjusting the set-up has been the choice of the chopper frequency, the thermal length and the noise have to be considered. An high frequency doesn't permit to the material to cool down or heat up; a very low frequency implies lot of noise and large integration time, the noise is in fact inversely proportional to the frequency. Experimentally I looked at the noise in the signal at different frequencies in the range of the ones which I considered good compromises to satisfy the above explained issues. A frequency of 13 Hz produce the lowest noise.

A final solution adopted has been the insertion of a lens to focus the exciting

laser beam on the back of the prism, in order to increase the amount of energy per unit area, and in this way the signal produced. A long focal length has been chosen ($20cm$).

In figure 4.25 two pictures of the experimental set-up can be seen. The upper one includes the laser, the optical chopper and the polarization optics, while the lower picture the prism stage and the optics relative to the probe beam. A dedicated software routine in pascal language has been written. It collects a set of data from the lock-in amplifier for each angle and analyzes them statistically in order to give an estimate and an associated error of the signal.
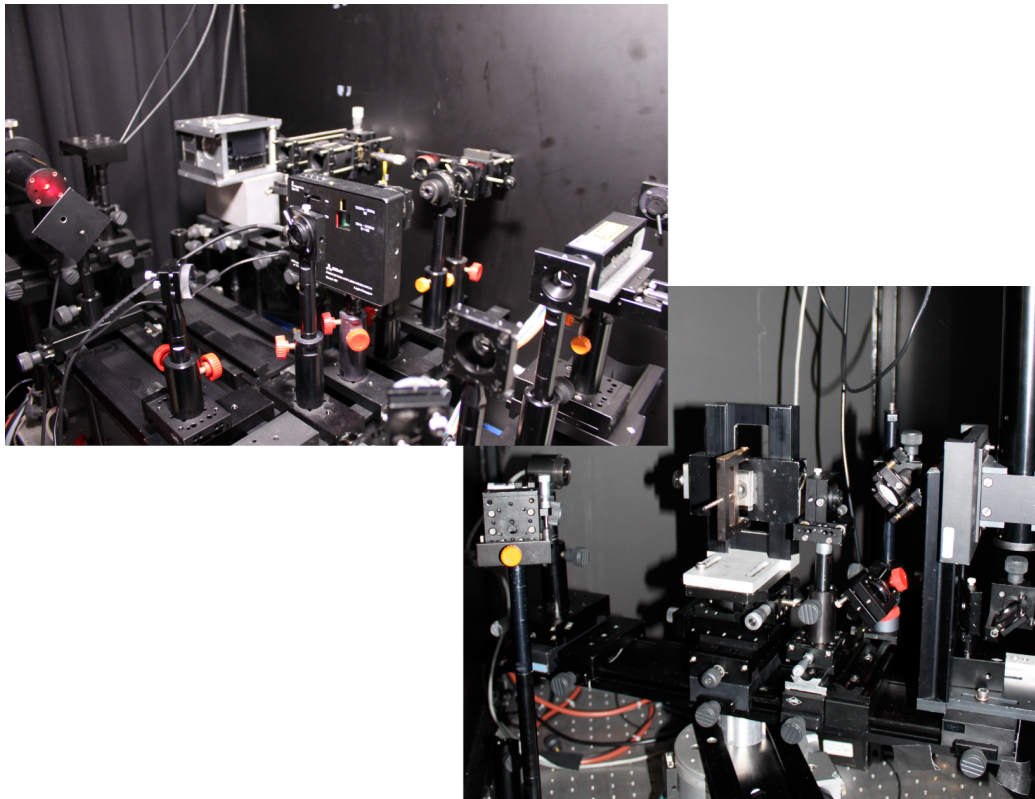
Figure 4.25: Pictures of the experimental set-up. In the upper part the excitation laser, the polarization optics and the mirrors to bend the beam into the dark chamber can be seen. In the lower part the attention is drown to the dark chamber where the prism, the detector and the probe beam with its optic are present.

Chapter 5

Results

5.1 Introduction

In the present chapter the main results obtained in my thesis work are presented. In the first section we deal with the Surface Plasmon Resonance experiment and the measurements for the gas sensing experiments are reported. In the following sections the results of the chromophores experiment are presented, in the second the theoretical calculations performed to prove the feasibility of this approach are presented, while in the third some experimental results are reported.

5.2 Gas sensing

Heating treatment on Au thin films deposited on glass substrate
The sol-gel deposition process requires the sample to be treated at high temperatures. For this reason the substrates prepared with the metal films have been subjected to an heat treatment in order to check how the SPR response changes. Samples available:

- n. 3 of 2 nm Cr + 52 nm Au deposited on August on BK7 glass;

- n. 2 of 2 nm Cr + 52 nm Au deposited on August on SF6 glass;

- n. 2 of 2 nm Cr + 52 nm Au deposited on May on BF33 glass.

The thickness values are the ones obtained through the microbalance which controls the deposition rate in the deposition chamber. One sample of each type has been heat treated in order to simulate the stress caused by the sol-gel deposition. The samples have been heated to $200°C$ for 30min, for two times: on Tuesday (06/09/07) and on Friday ((07/09/07). A series of measurements have been done for each sample to compare the SPR response just after the deposition and then after the first and the second heating cycle. The results are reported in figures 5.1,5.2,??.

Figure 5.1: Comparison of the SPR response of a sample before and after the first and the second heating. BF33 substrate.

As discussed in literature [40, 39, 29, 56] chromium may spread into gold when annealed at high temperature. In particular Y. Huang et al.[29] found that chromium atoms show significant diffusion in the Au layer when the annealing temperature reaches 200C and the annealing time exceeds 30 min;

Figure 5.2: Comparison of the SPR response of a sample before and after the first and the second heating. SF6 substrate.

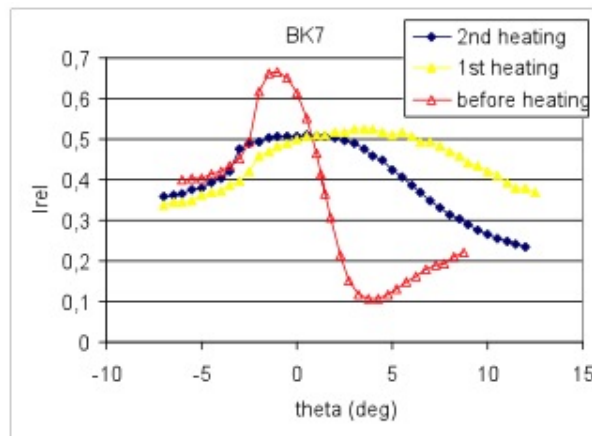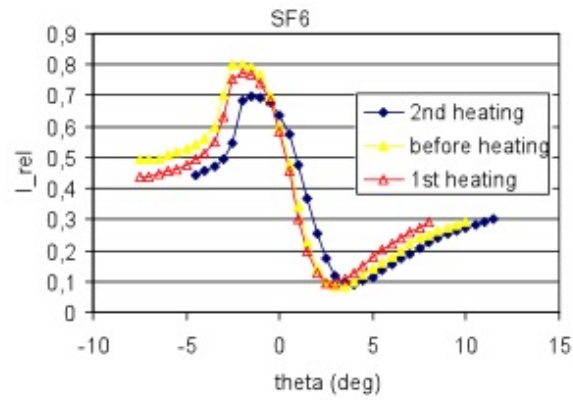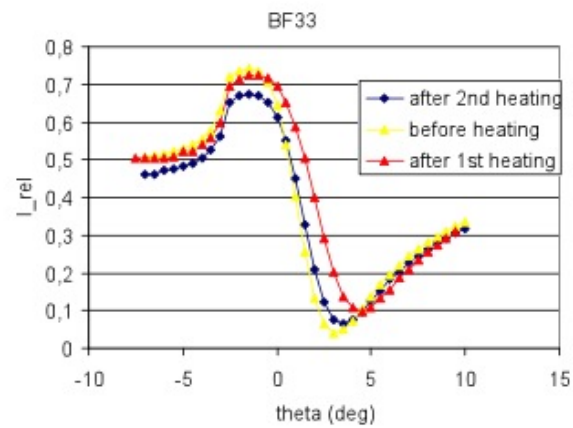**Figure 5.3:** Comparison of the SPR response of a sample before and after the first and the second heating. BF33 substrate.

and that when the annealing temperature rises to 250, chromium atoms have already diffused into the Au layer even for shorter annealing time of 5 min.

In the following several simulations are presented in order to investigate theoretically the influence of an intermixing layer on the SPR curve. The situation has been schematically described as depicted in figure 5.5.
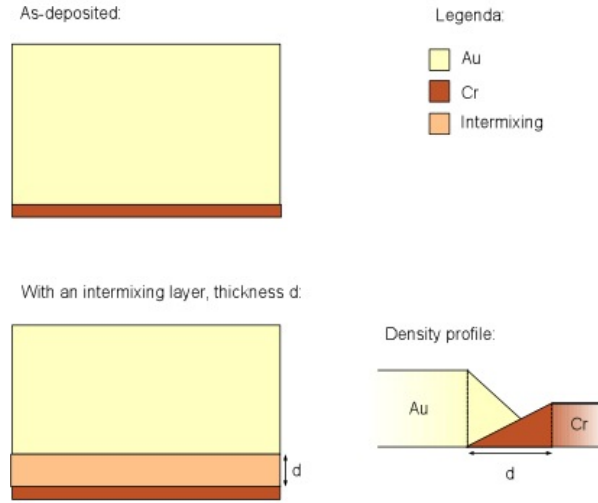
Figure 5.4: Schematic layout of the idea for the simulations of the mixing influence on the SPR response.

The optical constants (n, k) of the intermixing layer are derived weighting the optical constants of Au and Cr:

$$n_{intermixing\ layer} = (n_{Cr} \cdot \rho_{Cr} + n_{Au} \cdot \rho_{Au}); \tag{5.1}$$

$$k_{intermixing\ layer} = (k_{Cr} \cdot \rho_{Cr} + k_{Au} \cdot \rho_{Au}); \tag{5.2}$$

$$\rho_{Cr} + \rho_{Au} = 1. \tag{5.3}$$

The thicknesses of the pure Au and Cr layers are derived taking into account the thickness of the intermediate layer and the densities considered for the two materials and knowing that the total content of the two materials has to be preserved.
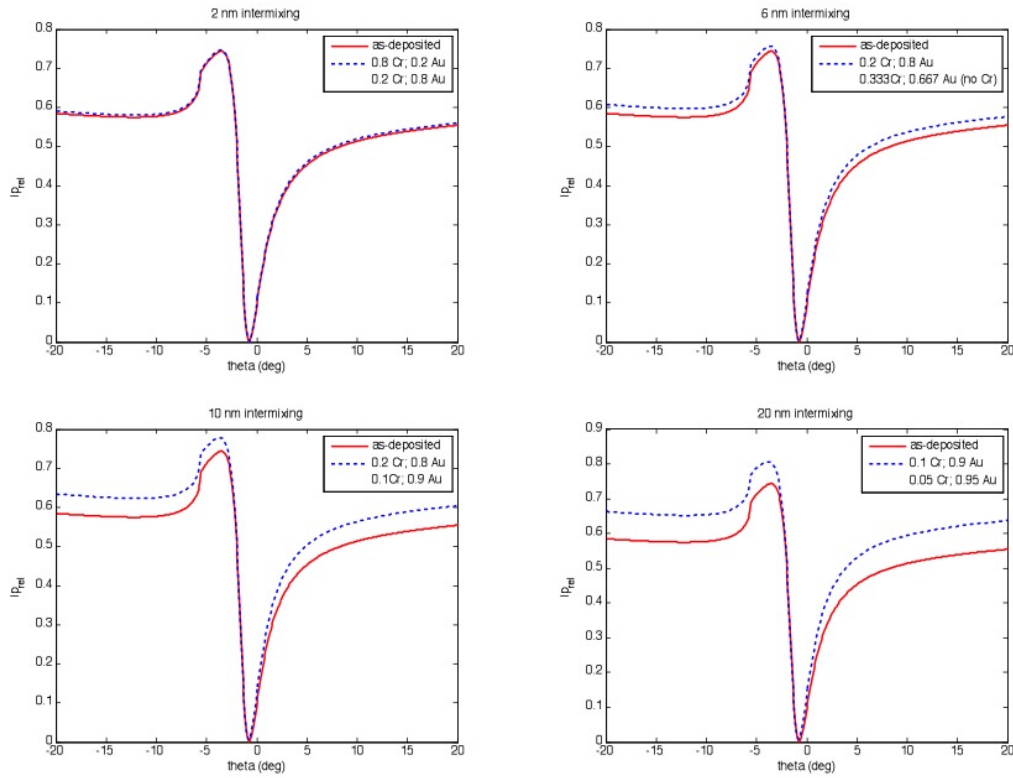
Figure 5.5: Simulations for different thicknesses of the intermixing layer are shown

In the following graphs the simulations results are shown. It has been assumed as wavelength $\lambda = 635$ nm, the optical constants are the ones of the literature and not fitted to our experimental results. Each graph corresponds to a defined thickness, d, of the intermixing layer and reports the results obtained for the different densities assumed.

It is evident that, when the intermixing layer becomes thicker, the maximum of reflectivity increases, this is probably due to the fact that Chromium tends to lower the reflectance. If instead of a defined chromium layer we consider a thick intermixing layer where the percentage of chromium has to be much lower than the Au one (for example see d = 20 nm case), the optical constants of this layer are much more similar to the Au ones and the

peak reflectance increases. This should not be a problem if the chromium reaches a stability point, because we could do an heat-treatment before the sol-gel film deposition. But it could be troublesome if the process of diffusion does not reach a stability point or if, as a consequence of this diffusion, the film adherence on the substrate changes (however P. T. Vianco et al.[56] in their work found that intermixing between the Cr and Au layers during heat treatment was not detrimental to the adhesive strength of the film).

Two different kinds of samples have been prepared for SPR measurements. One is a common gold thin film. The other one is a bimetallic structure composed by silver layer with a thin gold film on top. The simulations presented in chapter 2 show that the response of these bilayer depends on the ratio between the thickness of the two metal films. Bimetallic structures have already been used for SPR based fiber optic sensors [54], it has been pointed out that bimetallic configurations act better than single metal film in terms of sensitivity and resolution. In particular silver has a better resolution for SPR measurements, but it is not stable in air. Gold is instead more stable and has a greater sensitivity to changes of the refractive index. The thickness of the two stages has been chosen in order to obtain the sharper resonance as possible, in so far as structure stability allows. As usual a thin chrome layer is necessary in order to make the gold or the silver adhere to the glass substrate. TiO2 and TiO2-Au doped thin films have been eventually deposited onto this samples. In the following table structure parameters estimated in different ways are reported and compared. The first three columns refer to the thickness of the layers, estimated respectively with the microbalance in the deposition chamber, the ellipsometer and our SPR set-up.

These substrates have been used for the test with different gases. The sensing layers adhere to the long side of a BK7 rectangular prism through

an index matching fluid. A scheme of the sensing layer structure used in the presented measurements is shown in figure 5.6, it is the metal bi-layer with TiO2 on top.
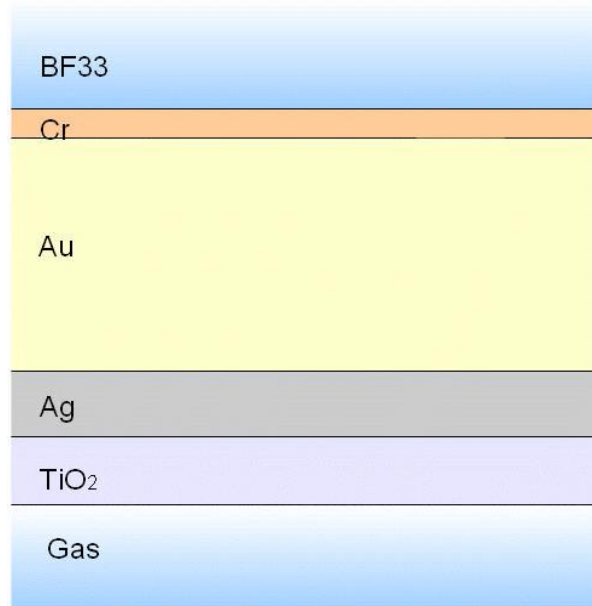
Figure 5.6: Schematic layout of the structure of the chip used for the gas detection measurement.

Before each test with an organic substance, a measure of nitrogen gas has been made as reference. Then the nitrogen gas has been made pass in a gas scrubber with the alcohol (ethanol, methanol or isopropanol) in it, in order

Table 5.1: estimates thickness and refractive index, Au

material	microbalance (nm)	elipsometer (nm)	spr (nm)	n @ 635nm
Cr	2	1.6	3	$3.6 \pm i4.36$
Au	53	46	49	$0.25 \pm i3.05$
TiO2	na	13(14)	12	1.71
TiO2 doped	na	11(12)	11	1.55

Table 5.2: estimates thickness and refractive index, Au/Ag

material	microbalance (nm)	elipsometer (nm)	spr (nm)	n @ 635nm
Cr	1.6	1.6	0.08	
Ag	53	46	49	$0.134 \pm \imath 4.21$
Au	6.1	6	6	$0.254 \pm \imath 3.764$
TiO2	na	14(15)	19	2
TiO2 doped	na	13(14)	19	1.72

to produce organic vapours. After the measurement, the sensing layer has been exposed to air for at least one day in order to free the alcohol molecules that could be entrapped in the sol-gel structure. In the following graphs the resonance curves obtained are presented.

The drifts are effectively due to the presence of the organic vapors. In
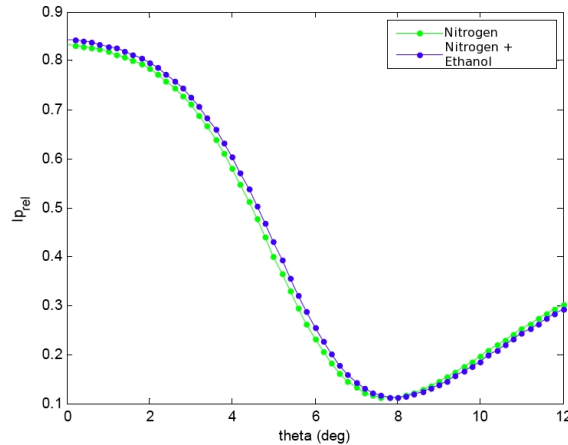
Figure 5.7: Ethanol. Comparison between the SPR scan on nitrogen and on N + C_2H_5OH.

order to verify this fact we have proved the repeatability of the measurement through the comparison between an angle scan performed before the gas measurements and one performed after them; as can be seen in fig. 5.10 they are superimposable.
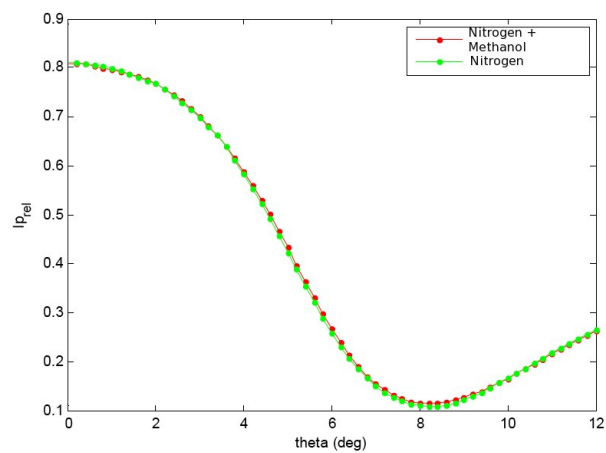
Figure 5.8: Methanol. Comparison between the SPR scan on nitrogen N and on N + CH_3OH.
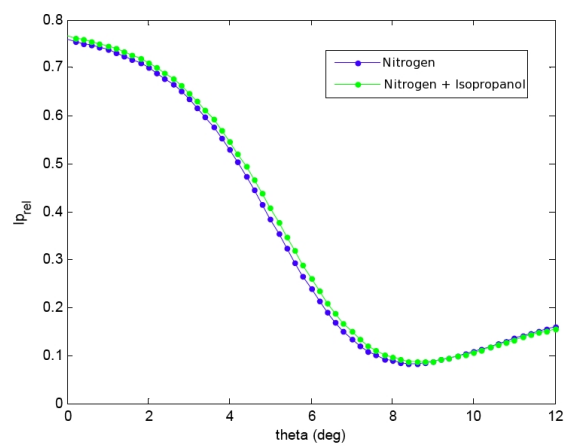
Figure 5.9: Isopropanol. Comparison between the SPR scan on nitrogen N and on N + C_3H_7OH.
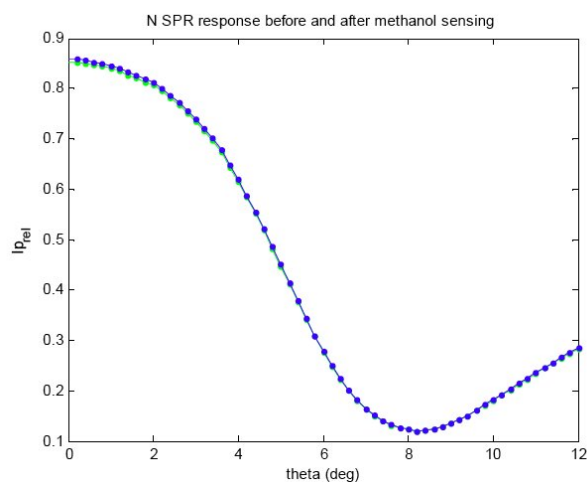
Figure 5.10: Angle scan before and after gas sensing to verify the repeatability of the measurement.

It has to be noted that it is only a qualitative test to see weather the layers are sensitive or not to the presence of the alcohol. It demonstrates that our samples are sensitive to the presence of the organic vapors and in a different way for every alcohol type, so that they could be used as substrates for selective measurements. For a more quantitative analysis, an independent gas concentration measurement should be performed.

5.3   Theoretical calculation on chromophores and local field

A theoretical calculation has been carried out in order to predict to which extent the effect is detectable in the measurement. The calculation has to take into account the absorbance (which can be measured with a UV-vis spectrometer), and relate it to the absorbance expected by the interaction of the chromophores with the local field at a the interface.

5.3.1 Cross section from UV-vis measurement

The absorption of the light is related to the properties of the material through which the light is traveling by the Beer-Lambert law

$$I_\lambda = I_\lambda^0 e^{-\alpha(\lambda)l} \tag{5.4}$$

The dimension of the absorption coefficient is

$$[\alpha(\lambda)] = \frac{1}{m} \tag{5.5}$$

Let N be the number of molecular entities contained in a unit volume (density). The cross section can be expressed in terms of the Neperian absorption coefficient

$$\sigma(\lambda) = \frac{\alpha(\lambda)}{N} \tag{5.6}$$

In the first instance the dependence on the wavelength is neglected and kept implicit. Comparing (5.6) with (5.4) and introducing the surface density factor N_A, one gets

$$\sigma = \frac{1}{N_A} \ln \frac{I_0}{I} \tag{5.7}$$

The absorbance, as the one measured by UV-vis is defined as

$$A = \log \frac{I_0}{I} \tag{5.8}$$

Inserting (5.8) in (5.7) we can derive the expression for the cross-section times the concentration as a function of the absorbance

$$N_A \sigma = \ln\left(10^A\right) = 2.3026 \cdot A \tag{5.9}$$

5.3.2 Power absorbed by chromophores

The supposed known parameters are
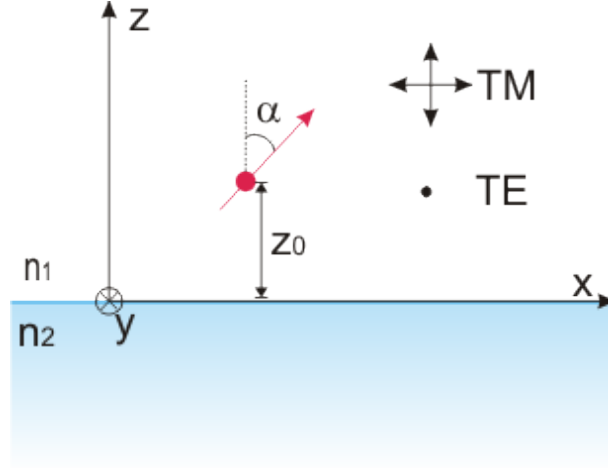
Figure 5.11: reference system

- Density $\times$ cross-section $(N\sigma)$;

- Orientation and distribution (initially supposed random);

- Local field $\rightarrow E = (E_x, E_y, E_z)$.

We wanto to relate the absorbed power to these parameters.

Let μ be the absorption dipole moment, n_μ its direction and α its polarizability. For weak excitation, the rate at which a two-level system is excited can be expressed as:

$$P' = \frac{\omega}{2} Im\{\alpha\} \left| \vec{n}_\mu \cdot \vec{E} \right|^2 \tag{5.10}$$

In order to obtain a rough estimate of the orders of magnitude, we can use the expression obtained through averaging on dipole orientation. Let n be the refractive index of the surrounding medium:

$$\sigma(\omega) = \frac{\langle P(\omega) \rangle}{I(\omega)} = \frac{\omega}{3} \sqrt{\frac{\mu_0}{\varepsilon_0}} \frac{Im\{\alpha(\omega)\}}{n(\omega)} \tag{5.11}$$

$$Im\{\alpha(\omega)\} = \frac{3}{\omega} \sqrt{\frac{\varepsilon_0}{\mu_0}} n(\omega)\sigma(\omega) \tag{5.12}$$

Substituting this expression in (5.10) one obtains for a single molecule:

$$P' = \frac{3}{2}\varepsilon_0 c n_2(\omega)\sigma(\omega)E_0^2\cos^2\theta. \tag{5.13}$$

For a volume $l \cdot dA$

$$P_{abs} = P' \cdot N_A \cdot dA \tag{5.14}$$

Assuming $P/dA = I$, we want to calculate the missing intensity in the reflected field in case of absorption of the local field by the chromophores. Let ϕ_{inc} be the angle of incidence of the beam:

$$I_{miss} = \frac{P_{abs}}{dA'} = P_{abs}\frac{cos\phi_{inc}}{dA} = \frac{3}{2}\varepsilon_0 c n_2\left(\sigma N_A\right)E_0^2 cos^2\theta cos\phi_{inc}. \tag{5.15}$$

The intensity of the incoming field, expressed in terms of the electrical field components is given by

$$I = \frac{n_1}{2}c\varepsilon_0\left|\rightarrow E\right|^2 \tag{5.16}$$

The ratio between I_{miss} (5.15) and the incident intensity (5.16) is then given by

$$\frac{I_{miss}}{I_{100\%}} = \frac{\frac{3}{2}\varepsilon_0 c n_2\left(\sigma N_A\right)E_0^2 cos^2\theta cos\phi_{inc}}{\frac{n_1}{2}c\varepsilon_0\left|\bar{E}\right|^2} = 3\frac{n_1}{n_2}A_{UV-vis}\frac{E_0^2}{E_{inc}^2}cos^2\theta cos\phi_{inc}. \tag{5.17}$$

Considering the order of magnitude of the different quantities that play a role in this equation, we see that the leading term is the absorbance A.

5.4 On-surface absorption

In this section we present some of the experimental results obtained with the photothermal deflection technique. We checked the final configuration of the set-up to be as stable as possible. The frequency of the chopper is set at 13 Hz. The signal to be detected is very low and can be buried by noise
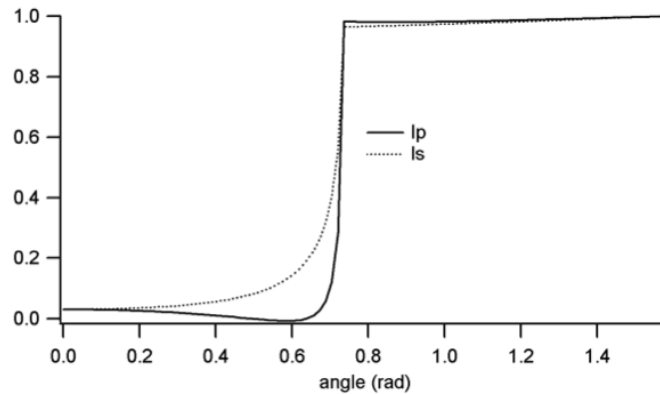
Figure 5.12: Total Internal Reflection, reflectivity as a function of the angle of internal incidence

even with this sophisticated configuration. For this reason the X and Y components computed from the incoming signal by the lock-in are recorded separately (see chapter 4). If there is random noise around zero R would record a certain value different from zero, while the X and Y components separately should average to zero. A statistical treatment of the recorded sets of data has to be performed in order to recover a reliable estimate of the signal.

A first test is meant to evaluate weather the experimental setup was able to detect the heat caused by absorption of the evanescent field in the back of the prism. A polished and cleaned as protocol BK7 slide has been painted with black permanent marker on one side. This slide has been coupled through index matching fluid to the base of the prism. The black paint is assumed as reference to have a nominal absorption $A = 100\%$. In figure 5.14 the response is shown. It is evident the difference in response in the case where the excitation laser is blocked and when it is impinging on the sample.

After this first evaluative test we passed to the measurement of sample with dyes. Several samples have been measured but the susceptibility of the
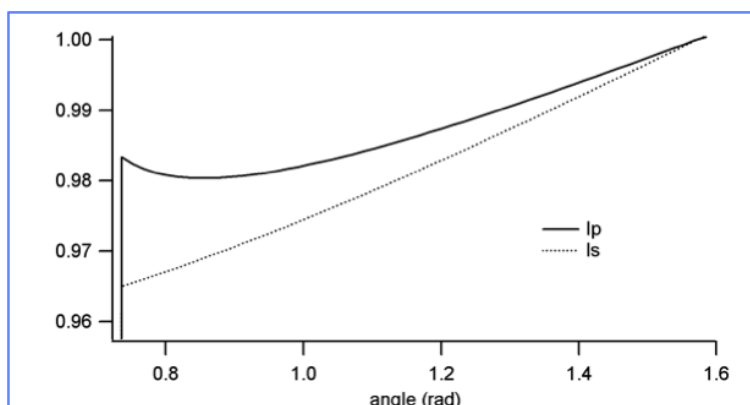
Figure 5.13: Total Internal Reflection. reflectivity as a function of the angle of internal incidence, Zoom near the edge.

measurement from the external influences and the weakness of the signal makes this kind of measurement difficult to perform. It is important to have a first characterization of the sample in terms of spectral response, in order to see weather it has a sufficient absorption at the wavelength of interest. Several types of dyes have been tested: Cy5, FL Red 646 Reactive, Atto633 NHS esther (Sigma Aldrich). In the following graphs we report the results for a couple of samples (S1 and S2), which have been prepared with two bilayers PSS-PAH and two bilayers PSS-PAH(Cy5 functionalized). Cy5 is a reactive water-soluble fluorescent dye of the cyanine dye family. It is fluorescent in the red region ($\sim$650/670 nm). In the first graph also the spectrum recorded through the UV-vis spectrometer is shown for both samples. For the sample S1 several consecutive measurements switching ON and OFF the excitation have been performed in order to see the changing in response with time, due to the low dye lifetime under light excitation.

Figure 5.14: The test response of the system with the black paint is shown. In the upper graph the X and Y components given by the lock in are separately shown, while in the second their quadratic sum R is presented.
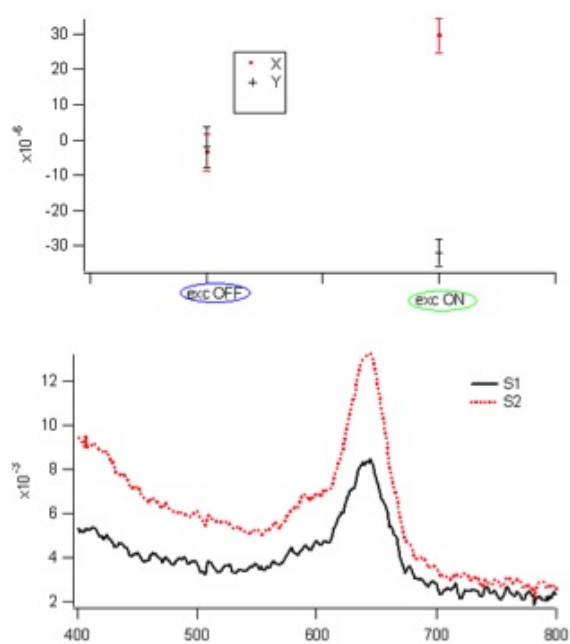
Figure 5.15: Test on sample S1 with dye
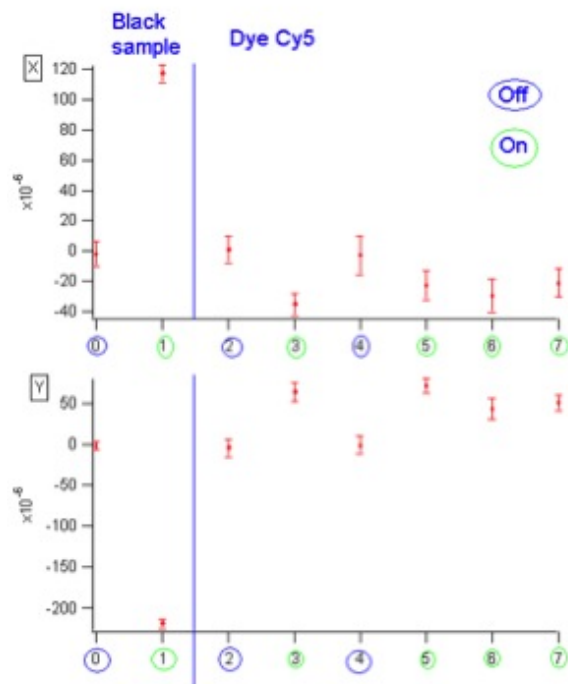
Figure 5.16: Test on sample S1 with dye
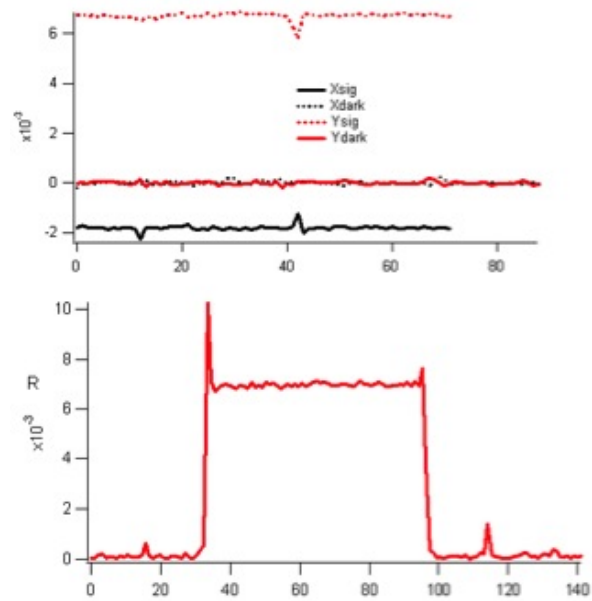
Chapter 6

Conclusions

Surface Plasmon Resonance   In the first part of my thesis i focused on the phenomenon of Surface Plasmon Resonance and its possible applications in detection of organic vapors. The comparison between calculated and experimental response has been also exploited to get the films parameters, i.e. thickness and index of refraction, both for the metal films and the TiO2 layers. I built an experimental bench set-up based on the Kretschmann configuration, the set-up has been tested and optimized. We have realized some different sensing layers for gas sensing. The outer gold film of the metal chips has been coated with a TiO2 or TiO2-Au doped layer. These layers have been deposited via sol-gel technique so that the porous structure would maximize the interactive area. The so structured chips have been tested on different kinds of organic vapors (methanol, ethanol and isopropanol). The tests on organic vapor demonstrate that the deposited layers are sensitive to the vapors in a selective way, it seems worth it to have also a precise independent measurement to calibrate the response of our films.

Chromophores   In the second part of my thesis I worked on the investigation of the local field behavior at an interface between two dielectrics. The local field is the evanescent field which is created in total internal reflection.

Theoretical calculations to estimate the effects on absorption and reflectivity of this interaction have been performed through a routine in an Igor PRO. environment. Results have been presented. I planned two different experimental approaches to detect the effects of the just mentioned interaction; they have been described, tested and discussed. The most successful experimental results are presented. The exerimental tests demonstrate the validity of the experimental configuration which bases its detection principle on the thermal lensing effect. The repeatability of the measurement needs still to be improved in order to have a systematic procedure of measurement.

Importance of photonics   Both experiments presented relate are aimed to provide new insights on photonic, in particular the SPR part concerns new methods for gas detection, while the chromophore experiment is more addressed to the understanding of the limits of the usual approach to the theoretical modeling of the nano-world. The importance of photonics nowadays can be seen from the multitude of application sectors where it is increasingly seen to be driving innovation. These sectors include information, communication, imaging, lighting, displays, manufacturing, life sciences and health care, and safety and security.

Chapter 7

Acknowledgemts

At the LUXOR lab in Padova I would like to thank Prof. Nicolosi and Dot.ssa Maria Guglielmina Pelizzo for their support and constructive discussions. Gianni Monaco for his help in the thin film deposition. All my other collegues, in particular Michele Suman and Fabio Frassetto, for the relaxing lunches and coffee breaks.

Thanks to Prof. Alessandro Martucci and Dr. Dario Buso of the Material Engineering Department of the University of Padova, they helped me in the sol-gel deposition.

I have to mention also my flatmates in Padova, Alessandro, Manu and Luca, who supported me in the difficult moments. Their company has always been a good healing ;)

In the last year and a half at the Max Plank Institute I had a great experience, i had the choice to work in an international environment, meeting very interesting people. I have to thank Dr. Max Kreiter and the other members the group for their help and fruitful discussions during the weekly seminar. A special thank to Janina Fisher, Nini, who helped me in the chemical lab.

Thanks to all the crew of the coffee corner for the amusement and the effort put in teaching me german.. With regard to this I would like to thank

also my german teacher, Eleni.

A special thank goes to Nuria Queralto, for her friendship and support when my motivation was diminishing. Thanks to Azhar Juhari, i will miss the musical breaks and conversations in his office. And of course to Ana, Marta and all my dear friends in Mainz.

Bibliography

[1] N. M. Aguirre, A. Passian, L. M. Perez, E. Lopez-Sandoval, C. Vazquez-Lopez, J. L. Jimenez-Perez, and T. L. Ferrell. The use of the surface plasmons resonance sensor in the study of the influence of "allotropic" cells on water. *Sensors and Actuators B-Chemical*, 99(1):149–155, 2004.

[2] M. L. Baesso, J. Shen, and R. D. Snook. Mode-mismatched thermal lens determination of temperature-coefficient of optical-path length in soda lime glass at different wavelengths. *Journal of Applied Physics*, 75(8):3732–3737, 1994. 25 AMER INST PHYSICS WOODBURY NG577.

[3] C. E. H. Berger and J. Greve. Differential spr immunosensing. *Sensors and Actuators B-Chemical*, 63(1-2):103–108, 2000.

[4] Max Born and Emil Wolf. *Priciples of Optics*. Pergamon Press, 6th corrected ed., reprinted edition, 1984.

[5] J. M. Brockman, B. P. Nelson, and R. M. Corn. Surface plasmon resonance imaging measurements of ultrathin organic films. *Annual Review of Physical Chemistry*, 51:41–63, 2000.

[6] A. N. Broers, W. W. Molzen, J. J. Cuomo, and N. D. Wittels. Electron-beam fabrication of 80-a metal structures. *Applied Physics Letters*, 29(9):596–598, —1976—. Ch339 Times Cited:207 Cited References Count:18.

[7] F. Caruso, M. J. Jory, G. W. Bradberry, J. R. Sambles, and D. N. Furlong. Acousto-optic surface-plasmon resonance measurements of thin films on gold. *Journal of Applied Physics*, 83(2):1023–1028, 1998.

[8] W. P. Chen and J. M. Chen. Use of surface plasma waves for determination of the thickness and optical constants of thin metallic films. *J. Opt. Soc. Am.*, 71(2):189–191, 1981.

[9] W.P Chen and J.M Chen. Surface plasma wave study of submonolayer cs and cs—o covered ag surfaces. *Surface Science*, 91(2-3):601 – 617, 1980.

[10] X. Chen and S. S. Mao. Titanium dioxide nanomaterials: Synthesis, properties, modifications, and applications. *Chemical Reviews*, 107(7):2891–2959, 2007. Chen, Xiaobo Mao, Samuel S. 961 AMER CHEMICAL SOC WASHINGTON 188NM.

[11] M. Commandre and E. Pelletier. Measurements of absorption losses in tio2 films by a collinear photothermal deflection technique. *Applied Optics*, 29(28):4276–4283, 1990. 12 OPTICAL SOC AMER WASHINGTON EC961.

[12] Manera et al. Optical gas sensing of tio2 and tio2/au nanocomposite thin films. *Sensors and Actuators B: Chemical*, 132(1):107 – 115, 2008.

[13] U. Fano. The theory of anomalous diffraction gratings and of quasistationary waves on metallic surfaces (sommerfeld's waves). *Journal of the Optical Society of America*, 31(3):213–222, —1941—. 15 AMER INST PHYSICS MELVILLE V13BQ.

[14] E. B. Feresenbet, M. Busi, F. Ugozzoli, E. Dalcanale, and D. K. Shenoy. Influence of cavity depth on the responses of spr sensors coated with self-assembled monolayers of cavitands. *Sensor Letters*, 2(3-4):186–193,

2004. 26 AMER SCIENTIFIC PUBLISHERS STEVENSON RANCH 004PY.

[15] C. D. Fernandez, M. G. Manera, G. Pellegrini, M. Bersani, G. Mattei, R. Rella, L. Vasanelli, and P. Mazzoldi. Surface plasmon resonance optical gas sensing of nanostructured zno films. *Sensors and Actuators B-Chemical*, 130(1):531–537, —2008—. Fernandez, C. de Julian Manera, M. G. Pellegrini, G. Bersani, M. Mattei, G. Rella, R. Vasanelli, L. Mazzoldi, P. 32 ELSEVIER SCIENCE SA LAUSANNE 284CD.

[16] C. D. Fernandez, M. G. Manera, J. Spadavecchia, G. Maggioni, A. Quaranta, G. Mattei, M. Bazzan, E. Cattaruzza, M. Bonafini, E. Negro, A. Vomiero, S. Carturan, C. Scian, G. Della Mea, R. Rella, L. Vasanelli, and P. Mazzoldi. Study of the gas optical sensing properties of au-polyimide nanocomposite films prepared by ion implantation. *Sensors and Actuators B-Chemical*, 111:225–229, 2005. 18th Eurosensors Conference SEP 12-15, 2004 Rome, ITALY 22 ELSEVIER SCIENCE SA LAUSANNE Sp. Iss. SI 977RM.

[17] A. Garcia-Valenzuela, G. E. Sandoval-Romero, C. Sanchez-Perez, L. Castaneda, and A. Guadarrama-Santana. Dynamic angle-scanning reflectometer device. *Review of Scientific Instruments*, 77(6), 2006.

[18] P. A. Gass, S. Schalk, and J. R. Sambles. Highly sensitive optical measurement techniques based on acoustooptic devices. *Applied Optics*, 33(31):7501–7510, 1994.

[19] P. A. Gass, S. Schalk, and J. R. Sambles. Highly sensitive optical measurement techniques based on acoustooptic devices. *Applied Optics*, 33(31):7501–7510, 1994.

[20] II Gordon, J. G. and S. Ernst. Surface plasmons as a probe of the electrochemical interface. *Surface Science*, 101(1-3):499–506, —1980—.

1662222 Netherlands Proceedings of an International Conference on Non-Traditional Approaches to the Study of the Solid-Electrolyte Interface 24-27 September 1979 Snowmass, CO, USA 14.

[21] E. B. Graper. Charged particle flux generated by an electron-beam deposition source. *Journal of Vacuum Science and Technology*, 7(1):282, —1970—. F8925 Times Cited:8 Cited References Count:4.

[22] E. B. Graper. Evaporation characteristics of materials from an electron-beam gun. *Journal of Vacuum Science and Technology*, 8(1):333, —1971—. I3986 Times Cited:7 Cited References Count:6.

[23] E. B. Graper. Deposition of aluminum from an electron-beam source. *Journal of Vacuum Science and Technology*, 9(1):33, —1972—. M1493 Times Cited:7 Cited References Count:6.

[24] E. B. Graper. Evaporation characteristics of materials from an electron-beam gun .2. *Journal of Vacuum Science and Technology a-Vacuum Surfaces and Films*, 5(4):2718–2723, —1987—. Part 4 J2597 Times Cited:3 Cited References Count:2.

[25] R. J. Green, R. A. Frazier, K. M. Shakesheff, M. C. Davies, C. J. Roberts, and S. J. B. Tendler. Surface plasmon resonance analysis of dynamic biological interactions with biomaterials. *Biomaterials*, 21(18):1823–1835, 2000.

[26] S. Haemers, G. J. M. Koper, M. C. van der Leeden, and G. Frens. An alternative method to quantify surface plasmon resonance measurements of adsorption on flat surfaces. *Langmuir*, 18(6):2069–2074, 2002.

[27] J. Homola. Present and future of surface plasmon resonance biosensors. *Analytical and Bioanalytical Chemistry*, 377(3):528–539, —2003—. 76 SPRINGER-VERLAG BERLIN BERLIN 724JZ.

[28] Jir Homola, Sinclair S. Yee, and Gnter Gauglitz. Surface plasmon reso-
nance sensors: review. *Sensors and Actuators B: Chemical*, 54(1-2):3 –
15, 1999.

[29] Y. Huang, H. Qiu, F. P. Wang, L. Q. Pan, Y. Tian, and P. Wu. Ef-
fect of annealing on the characteristics of au/cr bilayer films grown on
glass. *Vacuum*, 71(4):523–528, —2003—. 703DB Times Cited:8 Cited
References Count:12.

[30] M. C. Hutley. *Diffration gratings*. Academic Press, London, 1982.

[31] Charles Kittel. *Introduction to solid state physics*. Wiley, 2004.

[32] Kretschm.E and H. Raether. Radiative decay of non radiative sur-
face plasmons excited by light. *Zeitschrift Fur Naturforschung Part
a-Astrophysik Physik Und Physikalische Chemie*, A 23(12):2135, 1968.

[33] A. A. Kruchinin and Y. G. Vlasov. Surface plasmon resonance moni-
toring by means of polarization state measurement in reflected light as
the basis of a dna-probe biosensor. *Sensors and Actuators B-Chemical*,
30(1):77–80, —1996—. 10 ELSEVIER SCIENCE SA LAUSANNE LAU-
SANNE 1 UA677.

[34] B. C. Li, Y. Z. Deng, and J. Cheng. Sensitive photothermal interfero-
metric detection method for characterization of transparent plate sam-
ples. *Review of Scientific Instruments*, 67(10):3649–3657, —1996—. 38
AMER INST PHYSICS VN037.

[35] E. Maciak, Z. Opilski, T. Pustelny, and M. Bednorz. An optical detection
nh3 gas by means of a-wo3 thin films based on spr technique. *Journal
De Physique Iv*, 129:131–136, 2005. 34th Winter School on Wave and
Quantum Acoustics FEB 28-MAR 04, 2005 Ustron, POLAND Polish
State Comm Sci Res, Polish Acoust Soc, Upper Silesian Div, Silesian

Univ technol, Inst Phys 21 EDP SCIENCES S A LES ULIS CEDEX A 988QJ.

[36] M. G. Manera, G. Leo, M. L. Curri, P. D. Cozzoli, R. Rella, P. Siciliano, A. Agostiano, and L. Vasanelli. Investigation on alcohol vapours/tio2 nanocrystal thin films interaction by spr technique for sensing application. *Sensors and Actuators B-Chemical*, 100(1-2):75–80, 2004. Symposium on New Materials and Technologies in Sensor Applications JUN 10-13, 2003 Strasbourg, FRANCE European Mat Res Soc 15 ELSEVIER SCIENCE SA LAUSANNE 824IP.

[37] K. Matsubara, S. Kawata, and S. Minami. A compact surface-plasmon resonance sensor for measurement of water in process. *Applied Spectroscopy*, 42(8):1375–1379, —1988—. 11 SOC APPLIED SPECTROSCOPY FREDERICK R4717.

[38] M. Matsui, Y. Shiraki, E. Maruyama, and J. Ohwada. Thin-film transistors on molecular-beam-deposited polycrystalline silicon. *Journal of Applied Physics*, 55(6):1590–1595, —1984—. Sg987 Times Cited:19 Cited References Count:16.

[39] D. C. Miller, C. F. Herrmann, H. J. Maier, S. M. George, C. R. Stoldt, and K. Gall. Intrinsic stress development and microstructure evolution of au/cr/si multilayer thin films subject to annealing. *Scripta Materialia*, 52(9):873–879, —2005—. 902YW Times Cited:6 Cited References Count:33.

[40] N. R. Moody, D. P. Adams, D. Medlin, T. Headley, N. Yang, and A. Volinsky. Effects of diffusion on interfacial fracture of gold-chromium hybrid microcircuit films. *International Journal of Fracture*, 119(4-2):407–419, —2003—. 715DU Times Cited:10 Cited References Count:36.

[41] D. A. Nedosekin, M. Y. Kononets, M. A. Proskurnin, T. Y. Chaikovskii, and G. V. Lisichkin. Potential of thermo-optical methods for the study of molecular layers bonded to a flat glass surface. *Journal of Analytical Chemistry*, 62(2):126–135, 2007.

[42] Y. X. Nie and L. Bertrand. Separation of surface and volume absorption by photothermal deflection. *Journal of Applied Physics*, 65(2):438–447, 1989. 15 AMER INST PHYSICS WOODBURY R7204.

[43] C. Nylander, B. Liedberg, and T. Lind. Gas-detection by means of surface-plasmon resonance. *Sensors and Actuators*, 3(1):79–88, —1982—. 0 ELSEVIER SCIENCE SA LAUSANNE LAUSANNE PQ812.

[44] A. Otto. Excitation of nonradiative surface plasma waves in silver by method of frustrated total reflection. *Zeitschrift Fur Physik*, 216(4):398, 1968.

[45] M. C. Pena-Gomar, A. Garcia-Valenzuela, and M. Rosete-Aguilar. Design of an optical probe based on angle scanning reflectometry near the critical angle. *Optical Engineering*, 42(3):853–861, 2003.

[46] I. R. Pockrand and J. D. Swalen. Anomalous dispersion of surface plasma-oscillations. *Bulletin of the American Physical Society*, 23(3):278–278, —1978—.

[47] A. Pomozzi, M. K. Park, and M. Kreiter. Ensemble measurement of the orientation-dependent variations in chromophore lifetimes near a dielectric interface. *Physical Review B*, 79(16):8, 2009. Pomozzi, Andrea Park, Mi-Kyoung Kreiter, Maximilian Alexander von Humboldt Foundation M.- K. P. acknowledges the Alexander von Humboldt Foundation. 25 AMER PHYSICAL SOC COLLEGE PK 443XX.

[48] Andrea Pomozzi. *Fluorescence at dielectric interfaces*. PhD thesis, University of Mainz, 2009.

[49] M. A. Proskurnin and M. Y. Kononets. Modern analytical thermooptical spectroscopy. *Uspekhi Khimii*, 73(12):1235–1268, 2004. 598 MEZHDUNARODNAYA KNIGA 889CS.

[50] H. Raether. *Surface plasmons on smooth and rough surfaces and on gratings*. Springer-Verlag, 1988.

[51] R. Rella, A. Rizzo, A. Licciulli, P. Siciliano, L. Troisi, and L. Valli. Tests in controlled atmosphere on new optical gas sensing layers based on tio2/metal-phthalocyanines hybrid system. *Materials Science and Engineering C-Biomimetic and Supramolecular Systems*, 22(2):439–443, 2002. 8th European Conference on Organised Films SEP 03-07, 2001 OTRANTO, ITALY 7 ELSEVIER SCIENCE BV AMSTERDAM 627JJ.

[52] A. V. Samoylov, V. M. Mirsky, Q. Hao, C. Swart, Y. M. Shirshov, and O. S. Wolfbeis. Nanometer-thick spr sensor for gaseous hcl. *Sensors and Actuators B-Chemical*, 106(1):369–372, 2005. 15 ELSEVIER SCIENCE SA LAUSANNE 924VW.

[53] F. Sato, L. C. Malacarne, P. R. B. Pedreira, M. P. Belancon, R. S. Mendes, M. L. Baesso, N. G. C. Astrath, and J. Shen. Time-resolved thermal mirror method: A theoretical study. *Journal of Applied Physics*, 104(5):9, —2008—. Sato, F. Malacarne, L. C. Pedreira, P. R. B. Belancon, M. P. Mendes, R. S. Baesso, M. L. Astrath, N. G. C. Shen, J. 21 AMER INST PHYSICS 357NO.

[54] A. K. Sharma and B. D. Gupta. On the performance of different bimetallic combinations in surface plasmon resonance based fiber optic sensors. *Journal of Applied Physics*, 101(9), 2007.

[55] T. Turbadar. Complete absorption of light by thin metal films. *Proceedings of the Physical Society of London*, 73(469):40–44, —1959—. 4 IOP PUBLISHING LTD BRISTOL WM982.

[56] P. T. Vianco, C. H. Sifford, and J. A. Romero. Resistivity and adhesive strength of thin film metallizations on single crystal quartz. *Ieee Transactions on Ultrasonics Ferroelectrics and Frequency Control*, 44(2):237–249, —1997—. Wr981 Times Cited:4 Cited References Count:19.

[57] J. Wang, T. Zhu, J. Q. Song, and Z. F. Liu. Gold nanoparticulate film bound to silicon surface with self-assembled monolayers. *Thin Solid Films*, 327:591–594, 1998. 8th International Conference on Organized Molecular Films AUG 24-29, 1997 PACIFIC GROVE, CALIFORNIA.

[58] C. I. Wong, H. P. Ho, K. S. Chan, S. Y. Wu, and C. L. Lin. Application of spectral surface plasmon resonance to gas pressure sensing. *Optical Engineering*, 44(12):6, 2005.

[59] R. W. Wood. On a remarkable case of uneven distribution of light in a diffraction grating spectrum. *Philosophical Magazine*, 4(19-24):396–402, —1902—. Wood, R. W. 1 TAYLOR and FRANCIS LTD ABINGDON V42EJ.

[60] L. M. Wu and A. Knoesen. Absolute absorption measurements in polymer films using photothermal deflection spectroscopy. In S. Ducharme, D. H. Dunlap, and R. A. Norwood, editors, *Conference on Organic Photorefractives Photoreceptors Waveguides and Fibers*, pages 308–311, Denver, Co, 1999. Spie-Int Soc Optical Engineering.

[61] S. R. Yeh and D. E. Falvey. Applications of photothermal beam deflection calorimetry to organic-photochemistry. *Journal of Photochemistry and Photobiology a-Chemistry*, 87(1):13–21, 1995.

[62] J. Zhang, Q. Li, X. W. Di, Z. L. Liu, and G. Xu. Layer-by-layer as-
     sembly of multicolored semiconductor quantum dots towards efficient
     blue, green, red and full color optical films. *Nanotechnology*, 19(43):7,
     —2008—. Zhang, Jun Li, Qian Di, Xiaowei Liu, Zhiliang Xu, Gang Na-
     tional Natural Science Foundation of China [20601012, 20601016]; Inner
     Mongolia University [10013-121008, 206043, 206077]; Educational De-
     partment of Inner Mongolia [NJZY07011] 26 IOP PUBLISHING LTD
     352HK.

[63] S. Zuccon, M. G. Pelizzo, P. Nicolosi, D. Buso, and A. Martucci. Differ-
     ent sensing layers for spr sensing of organic vapours - art. no. 70410z. In
     G. B. Smith and A. Lakhtakia, editors, *Conference on Nanostructured
     Thin Films*, volume 7041, pages Z410–Z410, San Diego, CA, —2008—.
     Spie-Int Soc Optical Engineering. Zuccon, S. Pelizzo, M. G. Nicolosi, P.
     Buso, D. Martucci, A. 4 BELLINGHAM BIO28.